의학박사 학위논문

Evaluation of Cerenkov luminescence imaging on brown adipose tissue using translocator protein targeting PET probe in the UCP1 reporter mouse

UCP1 리포터 유전자 동물에서 전이체 단백질 (TSPO) 표적 양전자단층촬영 프로브를 이용한 갈색 지방 조직의 체렌코프 발광 영상 평가

2023년 2월

서울대학교 대학원
의과학과 의과학전공
이 석 용

Ph.D. Dissertation of Biomedical Sciences

UCP1 리포터 유전자 동물에서 전이체 단백질 (TSPO) 표적 양전자단층촬영 프로브를 이용한 갈색 지방 조직의 체렌코프 발광 영상 평가

Evaluation of Cerenkov luminescence imaging on brown adipose tissue using translocator protein targeting PET probe in the UCP1 reporter mouse

February 2023

Graduate School of Medicine
Seoul National University
Biomedical Sciences

Seok-Yong Lee

UCP1 리포터 유전자 동물에서 전이체 단백질 (TSPO) 표적 양전자단층촬영 프로브를 이용한 갈색 지방 조직의 체렌코프 발광 영상 평가

지도교수 강 건 욱

이 논문을 의학박사 학위논문으로 제출함

2022년 10월

서울대학교 대학원
의과학과 의과학전공
이 석 용

이석용의 의학박사 학위논문을 인준함

2023년 1월

위 원 장 _____ (인)
부위원장 _____ (인)
위 원 _____ (인)
위 원 _____ (인)
위 원 _____ (인)

Evaluation of Cerenkov luminescence imaging on brown adipose tissue using translocator protein targeting PET probe in the UCP1 reporter mouse

Submitting a Ph.D. Dissertation of
Biomedical Sciences

October 2022

Graduate School of Medicine
Seoul National University
Biomedical Sciences

Seok-Yong Lee

Confirming the Ph.D. Dissertation written by
Seok-Yong Lee
January 2023

Chair _____(Seal)
Vice Chair _____(Seal)
Examiner _____(Seal)
Examiner _____(Seal)
Examiner _____(Seal)

ABSTRACT

Seok-Yong Lee
Department of Biomedical Sciences
The Graduate School
Seoul National University

Introduction: [^{18}F]Fluoro-2-deoxyglucose ([^{18}F]FDG)-positron emission tomography (PET) has been widely suggested diagnostic imaging tool for measuring glucose uptake in adipose tissues, especially interscapular brown adipose tissue (iBAT). However, [^{18}F]FDG-PET was difficult to obtain the activity of iBAT because higher glucose uptake in the brain or heart interferes with iBAT imaging. Uncoupling protein 1 (UCP1) is well-known as a biomarker of iBAT, and a reporter mouse that can monitor UCP1 expression was recently developed. The translocator protein-18 kDa (TSPO) is located in the mitochondria membrane along with UCP1 and is overexpressed in iBAT. In addition, the TSPO targeting probe such as deuterium-substituted [^{18}F]fluoromethyl-PBR28-d_2 ([^{18}F]fm-PBR28-d_2) has been proposed to visualize iBAT. The non-invasive Cerenkov luminescence imaging (CLI) using Cerenkov radiation from PET radiotracer has been developed as an alternative optical imaging for PET due to less expensive and user-friendly. However, there are

no studies on the relationship between UCP1 expression and [^{18}F]FDG /or [^{18}F]fm-PBR28-d_2 uptake by comparing PET imaging and CLI. Here, I aim to evaluate the [^{18}F]FDG uptake or [^{18}F]fm-PBR28-d_2 binding for iBAT with PET imaging and CLI in UCP1 reporter mouse.

Methods: UCP1 reporter mouse was established by the insertion of a Luciferase2 (Luc2)-T2A-tdTomato cassette into the initiation codon of the *Ucp1*-coding sequence in exon 1. Bioluminescence imaging (BLI) and fluorescence imaging (FLI) were performed with IVIS 100. Western blotting and immunohistochemistry (IHC) were performed to measure UCP1, Luciferase, and TSPO levels. To visualize UCP1 expression in iBAT, [^{18}F]FDG-PET/CLI and [^{18}F]fm-PBR28-d_2-PET/CLI (TSPO-PET/CLI) were conducted. PET scans were acquired by small animal PET imaging (SimPET) and CLI was acquired using IVIS 100 after injection of [^{18}F]FDG or [^{18}F]fm-PBR28-d_2. To investigate qualitative differences in iBAT images between probes with different molar activity (A_m) of [^{18}F]fm-PBR28-d_2 for PET and CLI, one with high A_m and the other with low A_m of [^{18}F]fm-PBR28-d_2 were injected and compared. To determine the change of iBAT targeting imaging under physiological conditions, UCP1 reporter mouse was divided into cold and thermoneutral groups for 4 h. To verify the iBAT targeting imaging

by anesthesia exposure, I divided the UCP1 reporter mouse into a short exposure group and a long exposure group based on 2 h. PET images were reconstructed and analyzed by the AMIDE program. BLI, FLI, and CLI signals were obtained and analyzed with Living Imaging software.

Results: UCP1, luciferase, and TSPO expression in iBAT were correlated and significantly higher than in other adipose tissues. [^{18}F]FDG-PET/CLI signals were observed in iBAT but were also observed in the brain and heart. However, TSPO-PET/CLI signals were strongly detected in iBAT without its uptake in the brain and heart. [^{18}F]FDG-PET/CLI signals showed no difference between groups with different UCP1 levels. However, TSPO-PET/CLI signals were significantly higher in the group of high UCP1 levels and were lower in the group of low UCP1 levels. High molar activities group of TSPO-PET/CLI images were clearly detected in iBAT. Conversely, images from the low molar activities group of TSPO-PET/CLI images were poorly detected in iBAT. [^{18}F]FDG-PET/CLI signals were higher in the cold stimulation group than the thermoneutral condition group. However, the TSPO-PET/CLI signal showed more sensitive and specific differences between the cold stimulation group and the thermoneutral condition group. In the case of [^{18}F]FDG, there was no significant differences in both PET and CLI signals between

the two groups with different exposure terms to anesthesia. Interestingly, TSPO-PET/CLI signals were much higher in the t-term anesthesia exposure group than the long-term anesthesia exposure group.

Conclusion: UCP1 reporter mouse is a suitable *in vivo* model for monitoring UCP1 expression in the iBAT. My study was the first to evaluate CLI using a TSPO-targeting probe compared to [^{18}F]FDG for iBAT imaging. These results revealed that the TSPO targeting probe, [^{18}F]fm-PBR28-d_2 can be used as a reliable and sensitive probe for iBAT imaging than [^{18}F]FDG. Moreover, TSPO-CLI could be used as an alternative optical imaging technique to TSPO-PET for iBAT imaging.

Keywords: [^{18}F]fluoro-2-deoxyglucose, Positron emission tomography, Uncoupling protein 1, Translocator protein, Cerenkov luminescence imaging, UCP1 reporter mouse

Student number: 2017-25451

Table of Contents

LIST OF FIGURES AND TABLES

LIST OF ABBREVIATIONS

A_m, Molar activity

BLI: Bioluminescence imaging

BMI, Body mass index

CLI: Cerenkov luminescence imaging

CT, Computed tomography

DIO, Diet induced obese

eWAT: Epididymal white adipose tissue

FLI: Fluorescence imaging

UCP1, Uncoupling protein 1

TSPO, Translocator protein−18 kDa

iBAT, Interscapular brown adipose tissue

IHC: Immunohistochemistry

iWAT: Inguinal white adipose tissue

PET, Positron emission tomography

ROI, Region of interest

SUV, Standardized uptake value

SD, Standard deviation

[^{18}F]FDG, [^{18}F]fluoro−2−deoxyglucose

[^{18}F]fm−PBR28−d_2, deuterium−substituted [^{18}F]fluoromethyl−PBR28−d_2

CHAPTER 1

Evaluation of TSPO-targeting PET probe as bioimaging marker for BAT using PET and CLI

INTRODUCTION

1.1. Study Background

Obesity is a serious public health problem affecting nearly 40% of the world's population and is associated with insulin resistance, impaired glucose metabolism (e.g., type 2 diabetes mellitus), inflammation, and cancer [1−4]. Sarcopenic obesity, one of the diseases related to obesity, is defined as an imbalance in body fat mass compared to muscle mass, and its prevalence is mainly seen in the elderly, where obesity rates increase but muscle mass decreases [5]. To date, the common diagnostic indicator of adipose tissue (AT) is evaluated AT accumulation and overweight and obesity by body mass index (BMI) based on the weight of the person (kilogram, kg) and divided into the square height in meters (kg/m^2) [1, 2]. The World Health Organization (WHO) defines a person over 25 kg/m^2 is classified as overweight and over 30 kg/m^2 as obese [3]. Also, based on imaging methods, the thickness of fat is assessed by computed tomography (CT) [4, 6−8]. Recently, ATs are largely divided into white adipose tissue (WAT) and brown adipose tissue (BAT) [9]. The major role of WAT is to store fat, including large adipocytes and

a few mitochondria, but BAT has small adipocytes and many mitochondria [10-12]. In rodents, BAT depots are present in the cervical, axillary, mediastinum, and permanent depots. However, the largest BAT reservoir is located between the scapular (i.e., interscapular BAT, iBAT) [13, 14]. Among BATs, interscapular brown adipose tissue (iBAT) was first identified as a thermogenic organ in 1961 and is an organ that plays an important role in maintaining energy homeostasis and heat production called "non-shivering thermogenesis" [15-19]. Thus, impairment of the heat production and maintenance function of iBAT causes various metabolic diseases. As the importance of it has emerged, imaging modality for iBAT has been developed such as positron emission tomography (PET) using [^{18}F]fluoro-2-deoxyglucose ([^{18}F]FDG) [20-22]. In principle, [^{18}F]FDG is transported by glucose transporter 1 (GLUT1) which is located in the cell membrane and is phosphorylated by hexokinase 2 (HK2) which interacts with voltage-dependent anion channel 1 (VDAC1), the most abundant mitochondrial protein [23-25]. However, the [^{18}F]FDG is difficult to obtain iBAT-specific images in malignant tumors, inflammation, or during muscle activity [26]. Glucose uptake in iBAT is about 9.05-fold higher than in skeletal muscles but the total amount of it in the whole body is only 0.2 % of skeletal muscles. As a result, the amount

of total glucose uptake in iBAT was about 1% of that of skeletal muscles [27].

Uncoupling protein 1 (UCP1), also known as thermogenin, is most abundantly expressed in the mitochondrial inner membrane, and overexpressed in BAT compared to WAT used as its biomarker [20]. UCP1 uncouples the respiratory chain from oxidative phosphorylation and adenosine triphosphate (ATP) synthesis and uses it for energy. Proton leak (or uncoupled respiration) is H^+ as protons across the mitochondrial inner membrane and transported back into the mitochondrial matrix. However, in the process of bypassing ATP synthase, the energy derived from the oxidative of a substrate can be wasted and released as heat when protons return to the matrix [28-30]. In BAT, UCP1 has transported protons, which leads to an increase of protons in the mitochondrial inner membrane [31]. WAT depot under cold exposure or other chemical stimulation induces beige or brite (brown-in-white) which is UCP1 expressing adipocytes [11, 32, 33]. Therefore, BAT plays a pivotal role to generate heat by non-shivering thermogenesis. In 2014, a UCP1 reporter mouse (also known as ThermoMouse) capable of monitoring UCP1 expression in real-time was developed [34]. UCP1 reporter mouse is useful for obtaining bioluminescence and fluorescence

imaging by inserting luciferase2 (Luc2)-T2A-tdTomato cassette into exon1 of the UCP1 gene at the initiation codon. This reporter mouse model showed expression not only in BAT but also expressing UCP1 including WAT by three-dimensional imaging of the IVIS Spectrum Imaging System. However, UCP1 reporter mouse showed a significantly superior signals in iBAT than other WATs. Although various U.S. Food and Drug Administration (FDA) -approved drugs modulate UCP1 expression in BAT, no ligands that directly target UCP1 have not been developed [35]. Therefore, continued development of ligands targeting novel biomarkers for iBAT-specific imaging is required.

Translocator protein-18 kDa (TSPO), along with UCP1, is a five-transmembrane protein located on the mitochondrial outer membrane [36]. Representatively, TSPO is overexpressed during the neuroinflammatory response in glial cells so that used as an imaging target protein in various patients of brains such as neurodegenerative diseases [37, 38]. Various radioligands targeting TSPO as PET probes have been developed and used for imaging neuroinflammation [39-43]. Recently, TSPO is emerging as a potential biomarker for BAT imaging because it is overexpressed in BAT compared to WAT [44, 45]. According to many reports,

successful iBAT-PET using various TSPO radioligands in mice [44, 46, 47]. In 2018, there was the first report that successfully imaged human BAT using [^{11}C]PBR28 targeting TSPO [48]. However, this study could not provide BAT imaging data under cold stimulation reflecting physiological conditions. Deuterium-substituted [^{18}F]fluoromethyl-PBR28-d_2 ([^{18}F]fm-PBR28-d_2) was developed to overcome the increased metabolic stability and short half-life of [^{11}C] ($T_{1/2}$ = 20.36 min) [49]. However, clearly explained mechanisms for the association between UCP1 and TSPO expression have not been understood.

Although PET is a widely used diagnostic tool, PET requires an infrastructure for isotope supply and only 10% of countries have at least one scanner per million people [50]. As an alternative option to PET, CLI is an optical imaging technique to visualize charged particles of radionuclides such as [^{18}F], [^{131}I], [^{68}Ga], and [^{177}Lu] in the medium. Cerenkov luminescence (CL) is emitted when a velocity of charged particles (β^+ or β^-) goes through faster than the phase velocity of light in a dielectric medium [51, 52]. CLI is used in both preclinical and clinical studies because it can save scan time and is more cost-effective than PET for acquiring imaging [53-55]. CLI can determine the progress while monitoring the therapeutic

effectiveness of anti-cancer drugs, surgical resection, and endoscopic imaging in real-time [56, 57]. Recently, clinical trials to evaluate the correlation between CLI and PET images using β-emitting isotopes in patients with thyroid, neuroendocrine, and lymphoma and α-emitter $^{223}RaCl_2$ in patients for metastatic prostate cancer have been successfully conducted [58]. Considering this study, BAT has also been reported on successful CLI using [^{18}F]FDG [59-60]. However, these reports only show the distribution of [^{18}F]FDG based on anatomical location without comparing the expression of UCP1 with CLI.

1.2. Purpose of Research

In chapter 1, The main aim of this study is to investigate the expression of UCP1 with PET and CLI signals from iBAT using [^{18}F]FDG or [^{18}F]fm-PBR28-d_2 in UCP1 reporter mice. First, I evaluated whether the UCP1 reporter mouse is a suitable *in vivo* model for obtaining BAT imaging using BLI, FLI, and *ex vivo* organ distribution. In addition, Western blotting, and immunohistochemistry (IHC) were used to evaluate the TSPO as a potential imaging markers for iBAT imaging. Second, PET and CLI were used to compare the difference between [^{18}F]FDG or [^{18}F]fm-PBR28-d_2 in BAT. Third, I used TSPO-targeting probes with different molar activities to evaluate the quality of radioligands required for CLI image analysis as well as PET. I assessed the potential for optical imaging by observing the CLI of BAT with [^{18}F]FDG or [^{18}F]fm-PBR28-d_2 in all images except the characterization of the UCP1 reporter mouse.

MATERIALS AND METHODS

1. Animals

All experiments were approved by the Institutional Animal Care and Use Committee (IACUC) of the Seoul National University. UCP1 ThermoMice were purchased from Jackson Laboratory and carrier males were mated with FVB/NJ female mice to maintain live pubs. Since the reporter transgene was inserted into the Y chromosome, we used males aged 8-16 weeks old in this study. I described images of the reporter gene construct of the UCP1 reporter mouse (**Figure 1-1**).

2. Western blotting

Tissues (eWAT, iWAT, epididymis, iBAT, testis, and brain) were lysed by radio-immunoprecipitation assay buffer (RIPA) with a protease inhibitor cocktail and phenylmethylsulfonyl fluoride (PMSF). Lysates were centrifuged at 13,000 rpm for 20 min at 4 ℃. Protein concentrations were quantified by bicinchoninic acid (BCA) protein assay kit. Total proteins (10 μg) were separated on bis-Tris-HCl buffered 10% sodium dodecyl sulfate (SDS)-polyacrylamide gels. Separated proteins were transferred to a

polyvinylidene difluoride membrane (PVDF). Transferred membranes were blocked with 5% skim milk in Tris-buffered saline containing Tween-20 (Tris 20 mM, sodium chloride 138 mM, and 0.1% Tween-20 at pH 7.4) for 1 h room temperature. Membranes were incubated overnight at 4 ℃ with anti-UCP1 (ab10983, Abcam, Cambridge, UK), anti-TSPO (ab109497, Abcam, Cambridge, UK) and anti-β-actin (A5441, Sigma-Aldrich, St. Louis, MO, USA). Antigen-antibody complexed membranes were incubated for 1 h at room temperature with horseradish peroxide (HRP)-linked goat anti-rabbit IgG (7074S, Cell signaling Technology, Danvers, MA, USA) and horse anti-mouse IgG (7076S, Cell signaling Technology, Danvers, MA, USA). All intensities of immunoreactive chemiluminescence bands were visualized by the LAS-3000 imaging system (Bio-Rad Laboratories, Hercules, CA, USA).

3. Immunohistochemistry

Tissues (iWAT, eWAT, iBAT) were extracted from UCP1 ThermoMice and fixed with 4% paraformaldehyde (PFA). Fixed tissues were embedded in paraffin and the sectioned 4 μm slices were mounted on the glass slide. Mounted tissues on the glass were deparaffinized with xylene and ethanol, rehydrated, and incubated with 0.5% H_2O_2 (386790, Calbiochem, San Diego, CA, USA) for 30

min to block endogenous peroxidase. The slides were boiled with 10 mM sodium citrate at pH 6.0 for heat-induced epitope retrieval (HIER) and rinsed with 0.5% triton-X 100 (35501, Yakuri pure chemicals, OSAKA, Japan) in TBS for 5 min. The slides were blocked with 3% horse serum for 30 min. Primary antibodies were diluted with TBS containing 1% bovine serum albumin (BSA) and incubated at 4 ℃ for overnight. The following antibodies were used; rabbit isotype control (02-6102, Invitrogen, Waltham, MA, USA), goat isotype control (31245, Invitrogen, Waltham, MA, USA), anti-UCP1 (ab10983, Abcam, Cambridge, UK), anti-luciferase (NB100-1677, Novus Biologicals, Centennial, CO, USA), and anti-TSPO (ab109497, Abcam, Cambridge, UK). Biotinylated horse anti-rabbit IgG (BA-1100, Vector Laboratories, Burlingame, California, USA) and horse anti-goat IgG (BA-9500, Vector Laboratories, Burlingame, California, USA) as secondary antibodies for 1 h at room temperature to immunolabeling. Avidin/Biotin (ABC) kit (PK-6100, Vector Laboratories, Burlingame, California, USA) was incubated for 1 h to amplify signals. Finally, 3, 3' -diaminobenzidine (DAB) (SK-4100, Vector Laboratories) was used to develop a complex of avidin/biotin peroxidase, and slides were counterstained with hematoxylin.

4. [^{18}F]fm-PBR28-d_2 radiochemistry

[^{18}F]fm-PBR28-d_2 was synthesized following the protocols described previously [49].

5. Biodistribution

[^{18}F]FDG and [^{18}F]fm-PBR28-d_2 were injected with 0.37 MBq in UCP1 reporter mouse (n = 3 for each group) intravenously. UCP1 ThermoMice were sacrificed after 1 h and organs including blood, muscle, bone, intestine, stomach, testes, spleen, kidney, liver, heart, lung, iWAT, eWAT, and iBAT. Each organ was weighed and radio-activities were measured by Cobra II gamma counter (Canberra Packard; Vaughan, Ontario, Canada). The radioactivity uptake in organs was expressed as the percentage of injected dose per gram (%ID/g).

6. *In vivo* bioluminescence imaging

UCP1 reporter mouse were injected with D-Luciferin (3 mg per mouse, #E1605, Promega, WI, USA) intraperitoneally and anesthetized with 1.5% isoflurane combined with oxygen. The bioluminescence signals were acquired using IVIS 100 imaging system (Xenogen, Alameda, CA, USA) and analyzed with Living imaging software (ver.2.50.2, Xenogen, Alameda, CA, USA). To quantify the emitted light from iBAT, regions-of-interest (ROI) was

drawn over the iBAT. I used the maximum acquired bioluminescence signals from iBAT from each UCP1 reporter mouse. Average radiance was expressed as photons per second per cm^2 per steradian (photons/s/cm^2/sr).

7. *In vivo* Cerenkov luminescence imaging

UCP1 reporter mice were anesthetized with isoflurane combined with oxygen during CLI and [^{18}F]FDG or [^{18}F]fm-PBR28-d_2 were injected with 11.8 to 14.8 MBq per UCP1 reporter mouse. Injected UCP1 ThermoMice were subjected CLI sequentially acquired every 5 min until 1 h following parameters: open filter, f/stop = 1, binning = 4 and field of view (FOV) = D. I used the maximum acquired Cerenkov luminescence signals from iBAT from each UCP1 reporter mouse. Average radiance was expressed as photons/s/cm^2/sr.

8. *In vivo* PET imaging

Small animal PET imaging (SimPET, BRIGHTTONIX imaging, Seoul, Republic of Korea) was used to visualize PET signals from iBAT in each group ([^{18}F]FDG or [^{18}F]fm-PBR28-d_2). UCP1 reporter mice were anesthetized with isoflurane combined with oxygen during the PET scans. Static PET images was acquired for

10 min and the images were reconstructed by three-dimensional ordered-subset expectation maximization (3D OSEM) algorithm. Analysis of PET images were performed using medical image data examiner (AMIDE) software (ver. 0.9.0, http://amide.sourceforge.net). An ellipsoidal ROI was drawn over the brain and iBAT to quantify PET signals. Quantified PET signals from ROI were expressed as a maximal standardized uptake value (SUV_{max}).

9. Statistical analysis

All results were expressed as mean ± standard deviation (SD) and statistical significance was determined by unpaired 2-sample parametric Student t-test using GraphPad Prism 8 software (GraphPad Software Inc., San Diego, CA, USA). Statistical significance was considered $P < 0.05$.

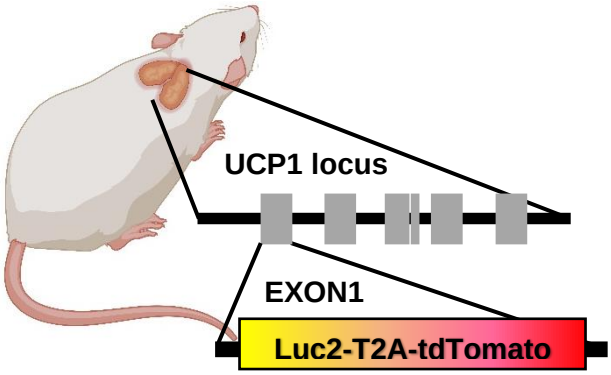

Figure 1. Design of reporter gene construct of UCP1 reporter mouse.

The luc2−T2A−tdTomato cassette was inserted into exon1 at the initiation codon in a 98.6 kb bacterial artificial chromosome (BAC) containing the entire *Ucp1* gene locus.

RESULTS

Characterization of UCP1 reporter mouse *in vivo* imaging

To characterize whether inserted Luc2-T2A-tdTomato transgene reflecting UCP1 expression in UCP1 reporter mouse is useful for imaging *in vivo* UCP1 expression from iBAT, I performed BLI and FLI using IVIS 100 (Xenogen, Alameda, CA, USA) for monitoring UCP1 expression. The bioluminescence and fluorescence signals from Luc2 activity and tdTomato were observed in iBAT (**Figure 1-2**). As shown in **Figure 1-3**, UCP1 expression in the whole-body organs of UCP1 reporter mouse showed specifically higher bioluminescence signals in iBAT and epididymis with testis than other organs. The epididymis protrudes above the testis and emits a relatively stronger bioluminescence signal because it is more adjacent to the detector than the flat iBAT. In principle, a shorter distance between the detector and the object appears to exaggerate the bioluminescence signal in the optical image. Also, I observed weak bioluminescence signals from brain which recently reported to be expressed UCP1.

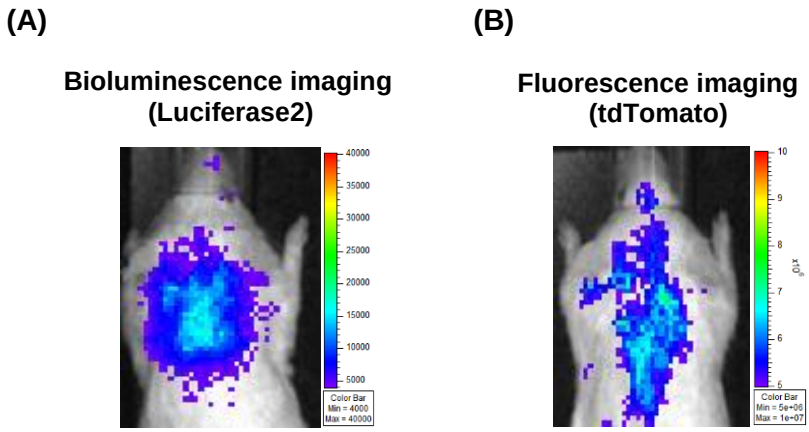

Figure 1-2. *In vivo* bioluminescence imaging (BLI) and fluorescence imaging (FLI).

(A) BLI from Luc2 signals of BAT in the UCP1 reporter mouse. (B) Fluorescence imaging from tdTomato signals of iBAT in UCP1 reporter mouse.

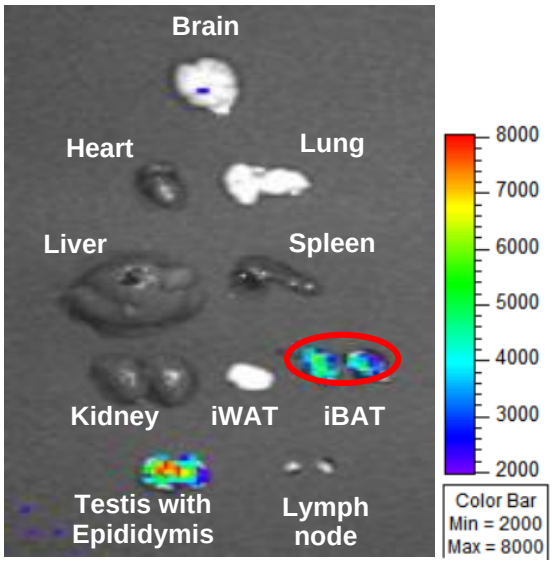

Figure 1-3. *Ex vivo* organ distribution. BLI for monitoring of UCP1 expression of whole-body organs from UCP1 reporter mouse.

Correlation between UCP1 and TSPO expression in iBAT

As mentioned above, UCP1 is a known biomarker for BAT. Recently, TSPO is also overexpressed in iBAT and TSPO-targeting radioligands have been suggested for iBAT-specific imaging [46-48]. I evaluated the expression correlation between UCP1 and TSPO in iBAT to determine whether it is suitable for obtaining images of iBAT in a UCP1 reporter mouse using a TSPO-targeting probe using Western blotting and IHC. **Figure 1-4A** shows higher expression of UCP1 and TSPO than other tissues. Consistent with **Figure 1-3**, higher UCP1 expression in the epididymis and brain was observed than in other WAT and testis. However, it is considered that there is no interference in animal imaging using UCP1 as a marker of iBAT because epididymis and iBAT are significantly separated in anatomical location. In addition, IHC staining of UCP1, luciferase , and TSPO increased expression in iBAT compared to inguinal white adipose tissue (iWAT) or epididymal white adipose tissue (eWAT) (**Figure 1-4B**).

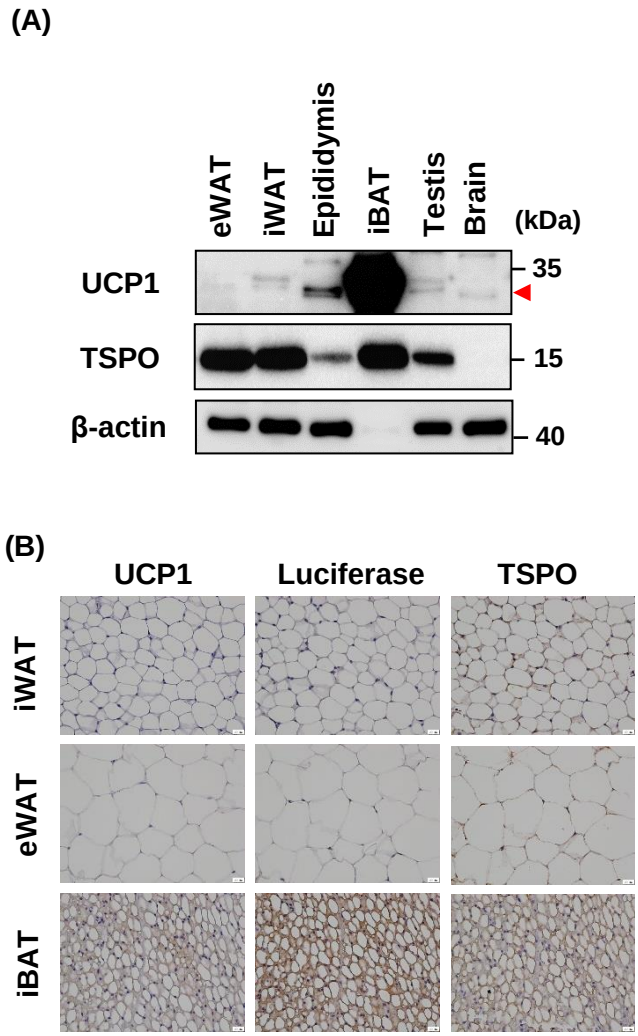

Figure 1−4. Correlation between UCP1 and TSPO in iBAT. (A) UCP1 and TSPO expression in various organs and different adipose tissues by Western blotting. (B) Expression of UCP1, luciferase and TSPO in iWAT, eWAT and iBAT. Slides were counterstained with hematoxylin. Scale bar, 20 μm.

PET and CLI imaging of iBAT with [^{18}F]FDG or [^{18}F]fm-PRB28-d_2 in UCP1 reporter mouse

To evaluate the possibility of CLI as an alternative option for iBAT-PET imaging, I tested PET/CLI of [^{18}F]FDG in UCP1 reporter mouse. [^{18}F]FDG uptake in iBAT was observed by PET and CLI, but also showed strong [^{18}F]FDG uptake in brain (**Figure 1-5A**). Quantitatively analysis of [^{18}F]FDG-PET imaging showed that [^{18}F]FDG uptake was 5.08-fold higher in brain than iBAT (SUV_{max}, brain *vs.* iBAT, 2.929 ± 0.7742 *vs.* 0.575 ± 0.058, $^{**}P = 0.0063$, **Figure 1-5B**). Consistent with [^{18}F]FDG-PET results, CLI signals was 1.5-fold higher in brain than iBAT (Average radiance, photon/s/cm^2/sr, brain *vs.* iBAT, 1,186,667 ± 80,829 *vs.* 791,000 ± 57,026.3, $^{**}P = 0.0023$, **Figure 1-5C**). These results suggested that [^{18}F]FDG uptake in brain than iBAT could interfere with obtaining iBAT-specific imaging.

Based on the results of **Figure 1-4 and 5**, TSPO-targeting probe ([^{18}F]fm-PBR28-d_2) was evaluated by PET and CLI for iBAT imaging. Contrary to the [^{18}F]FDG-PET/CLI results (**Figure 1-5**), PET and CLI were show [^{18}F]fm-PBR28-d_2 uptake is much higher in iBAT than brain (**Figure 1-6A**). Quantitatively analysis of [^{18}F]fm-PBR28-d_2-PET (TSPO-PET) showed that [^{18}F]fm-PBR28-d_2 uptake was 12.92-fold higher in iBAT than brain (SUV_{max},

iBAT *vs.* brain, 8.246 ± 0.688 *vs.* 0.637 ± 0.182, $^{****}P < 0.0001$, **Figure 1-6B**). Consistent with TSPO-PET results, [^{18}F]fm-PBR28-d_2-CLI (TSPO-CLI) signal was 1.93-fold higher in iBAT than brain (Average radiance, photon/s/cm^2/sr, iBAT *vs.* brain, 762,333.3 ± 68,995.2 *vs.* 395,000 ± 35,085.6, $^{**}P = 0.0012$, **Figure 1-6C**).

Finally, I performed biodistribution study using [^{18}F]FDG and [^{18}F]fm-PBR28-d_2 in the UCP1 reporter mouse. [^{18}F]FDG uptake in iBAT show significantly higher in heart and brain than [^{18}F]fm-PBR28-d_2 (%ID/g, [^{18}F]FDG *vs.* [^{18}F]fm-PBR28-d_2, 56.74 ± 10.6 *vs.* 15.88 ± 13.66, $^{*}P = 0.014$ for the heart; 6.62 ± 1.38 *vs.* 1.52 ± 0.96, $^{**}P = 0.0063$ for the brain). Significantly, [^{18}F]fm-PBR28-d_2 uptake in iBAT was much higher than [^{18}F]FDG (%ID/g, [^{18}F]FDG *vs.* [^{18}F]fm-PBR28-d_2, 7.68 ± 2.47 *vs.* 34.08 ± 6.32, $^{**}P = 0.0025$) (**Figure 1-7** and **Table 1**).

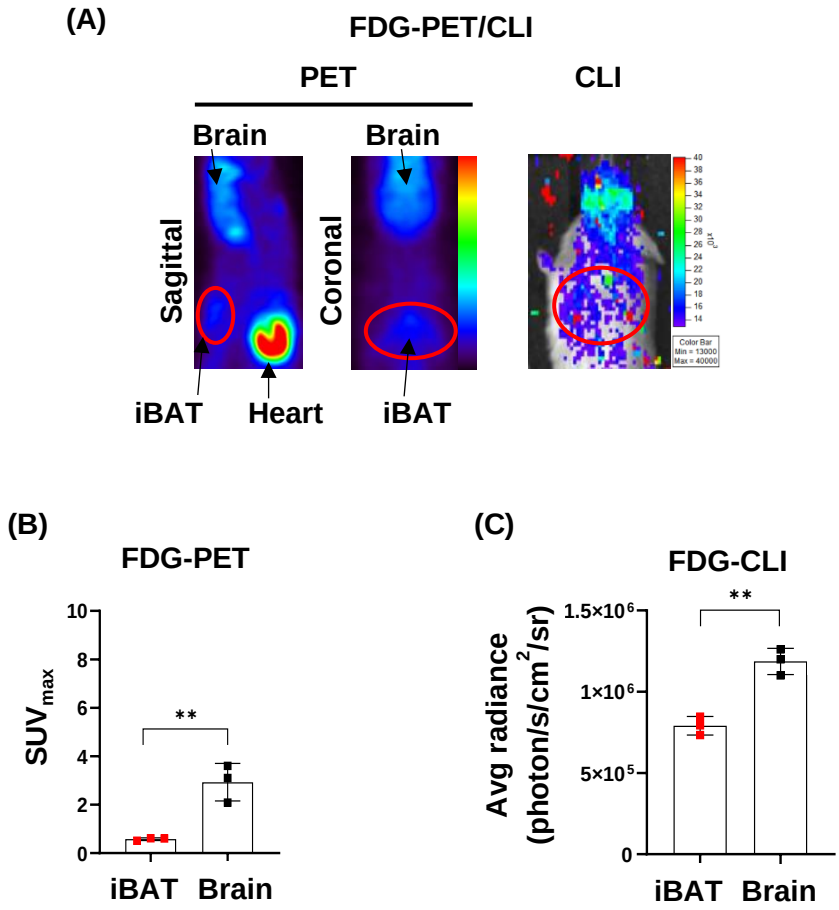

Figure 1-5. PET and CLI using [^{18}F]FDG for iBAT imaging in UCP1 reporter mouse. (A)Representative images of[^{18}F]FDG-PET/CLI. (B) Quantitative analysis of [^{18}F]FDG-PET signals (SUV_{max} ratio for PET) from iBAT and brain. (C) Quantitative analysis of [^{18}F]FDG-CLI (Average radiance for CLI) signals from iBAT and brain. Data represent mean ± SD (n = 3 per group). **P <0.01.

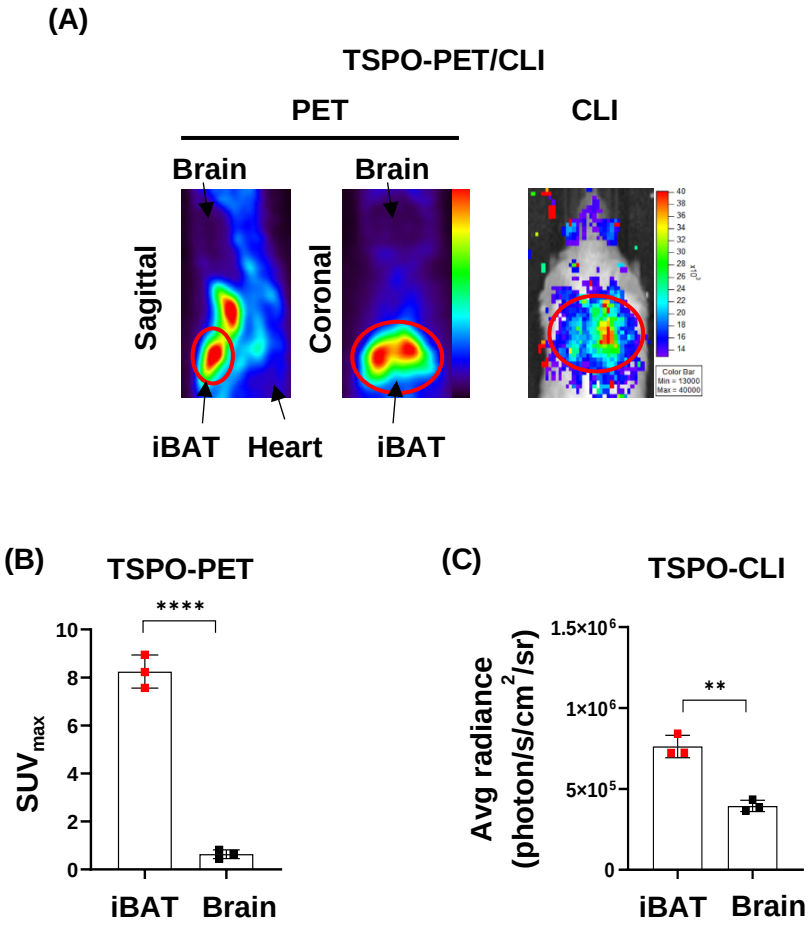

Figure 1-6. PET and CLI using [^{18}F]fm-PBR28-d_2 for iBAT imaging in UCP1 reporter mouse. (A)Representative images of TSPO PET/CLI. (B) Quantitative analysis of TSPO-PET signals (SUV_{max} ratio for PET) from iBAT and brain. (C) Quantitative analysis of TSPO-CLI (Average radiance for CLI) signals from iBAT and brain. Data represent mean ± SD (n = 3 per group). $^{****}P < 0.0001$.

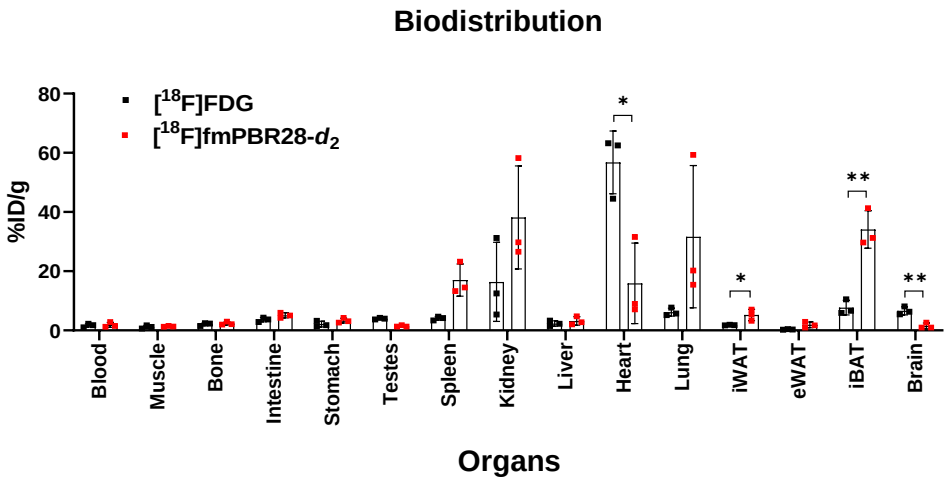

Figure 1-7. Biodistribution of [^{18}F]FDG and [^{18}F]fm-PBR28-d_2.

The biodistribution of [^{18}F]FDG and [^{18}F]fm-PBR28-d_2 uptake in UCP1 reporter mouse. Data represented mean ± SD (n = 3 per group). $^{*}P < 0.05$; $^{**}P < 0.01$

Table 1. Biodistribution of [^{18}F]FDG *vs.* [^{18}F]fm−PBR28−d_2.

%ID/g	[^{18}F]FDG		[^{18}F]fm−PBR28−d_2		
Organs	Mean	SD	Mean	SD	P−value
Blood	1.67	0.47	1.86	0.67	
Muscle	1.16	0.44	1.34	0.11	
Bone	2.08	0.42	2.34	0.20	
Intestine	3.61	0.60	5.08	0.71	
Stomach	2.14	0.79	3.31	0.68	
Testis	3.96	0.20	1.46	0.20	
Spleen	4.06	0.52	17.01	4.44	
Kidney	16.38	10.91	38.19	14.21	
Liver	2.33	0.75	3.18	1.16	
Heart	56.74	10.6	15.88	13.6	*
Lung	6.19	1.09	31.66	19.63	
iWAT	1.78	0.08	5.21	1.55	*
eWAT	0.33	0.08	1.87	0.81	
iBAT	7.68	2.47	34.08	6.32	**
Brain	6.62	1.38	1.52	0.96	**

(*$P < 0.05$; **$P < 0.01$; n = 3 per group)

Division of high or low endogenous UCP1 expression by BLI

As described above, because the transgene (Luc2-T2A-tdTomato) cassette was inserted into the Y chromosome [34], UCP1 expression varies between individual UCP1 reporter mice. The luciferase activity obtained by BLI was divided into a high-expression group and a low-expression group. Subsequently, [^{18}F]FDG and [^{18}F]fm-PBR28-d_2 were compared by PET and CLI between high and low groups. At first, bioluminescence signals reflecting endogenous UCP1 expression were 1.85-fold higher in the high group than in the low group. (Average radiance, photon/s/cm^2/sr, high *vs.* low, 4,435.6 ± 609.5 *vs.* 2,387 ± 542.83, ***P = 0.0005, Figure 1-8).

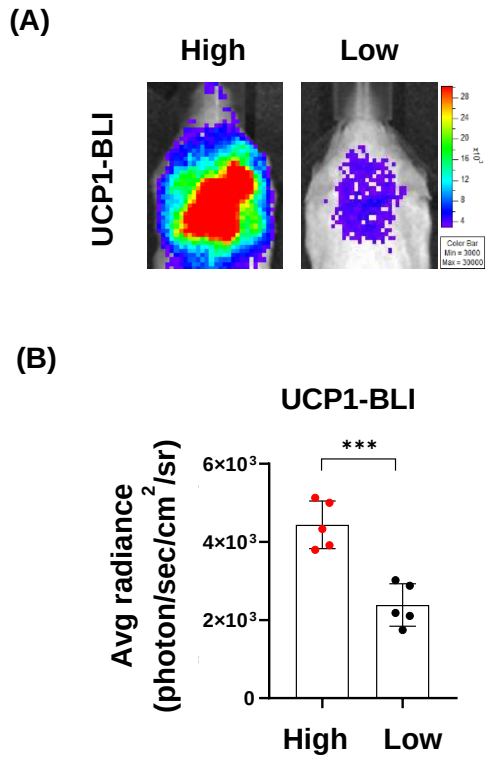

Figure 1-8. *In vivo* BLI between high and low endogenous UCP1 level group. (A) Representative bioluminescence images between high and low endogenous UCP1 expression group. (B) Quantitative analysis of UCP1-BLI signals from iBAT between high and high and low endogenous UCP1 expression group. Data represent mean ± SD (n = 5 per group). $^{***}P < 0.001$.

[^{18}F]FDG-PET/CLI and TSPO-PET/CLI with different group of endogenous UCP1 expression in UCP1 reporter mice

Thereafter, I observed [^{18}F]FDG-PET and [^{18}F]FDG-CLI in between the high and low groups. [^{18}F]FDG-PET and [^{18}F]FDG-CLI could not identify the difference between the high and low groups in iBAT with [^{18}F]FDG. (**Figure 1-9A**). Furthermore, quantitative analysis of [^{18}F]FDG-PET (SUV_{max}, high *vs.* low, 1.12 ± 0.46 *vs.* 0.86 ± 0.36, ns, **Figure 1-9B**) and [^{18}F]FDG-CLI did not show statistical significance between the high and low groups (Average radiance, photon/s/cm^2/sr, high *vs.* low, 13,534 ± 2,087.47 *vs.* 13,578 ± 2,613.71, ns, **Figure 1-9C**). Interestingly, **Figure 1-10A** shows that TSPO-PET and TSPO-CLI were significantly higher in the high group than the low group. Consistent with imaging data, quantitative analysis of TSPO-PET (SUV_{max}, high *vs.* low, 3.47 ± 0.99 *vs.* 1.40 ± 0.95, $^{*}P = 0.0104$, **Figure 1-10B**) and TSPO-CLI (Average radiance, photon/s/cm^2/sr, 16,422 ± 1,912.57 *vs.* 11,673 ± 2,655.12, $^{*}P = 0.012$, **Figure 1-10C**) was much higher in the high group than the low group. These data highlight that iBAT imaging of UCP1 reporter mouse using TSPO targeting probes rather than [^{18}F]FDG is more reliable.

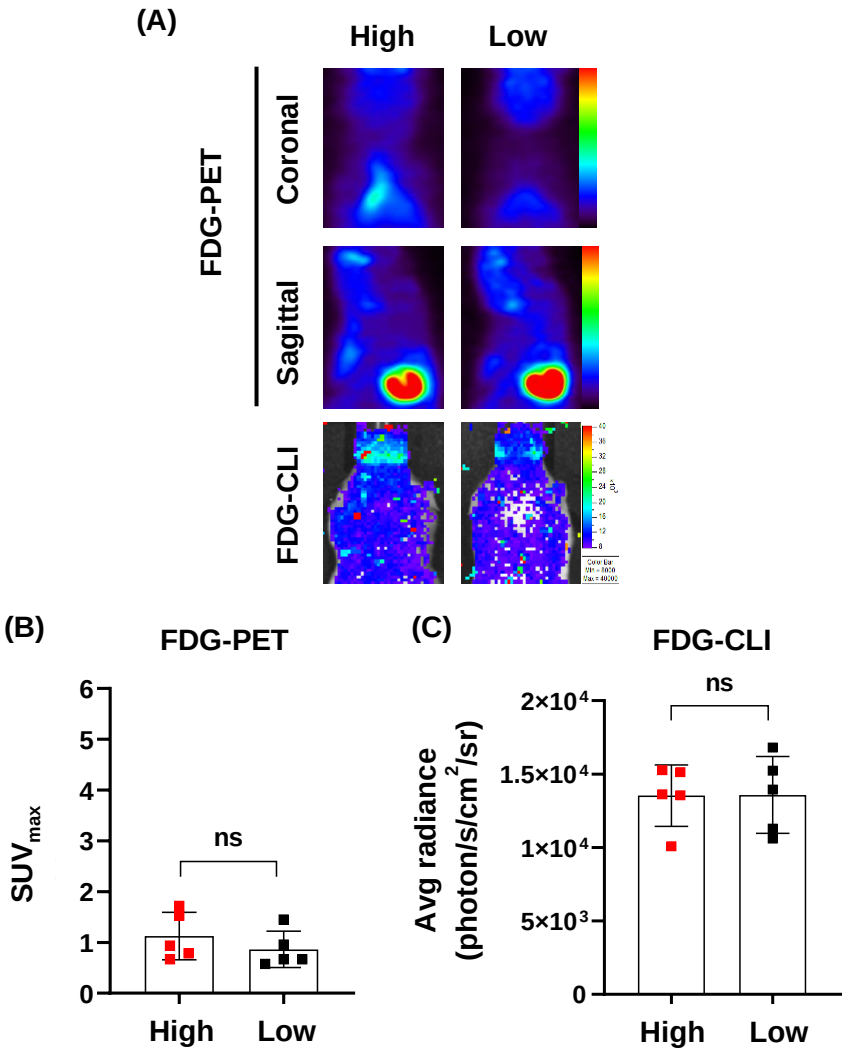

Figure 1-9. [^{18}F]FDG-PET and [^{18}F]FDG-CLI between high and low endogenous UCP1 level group. (A) Representative [^{18}F]FDG-PET and CLI images between high and low endogenous UCP1 level group. (B) Quantitative analysis of FDG-PET signals from iBAT between high and low endogenous UCP1 level group. (C) Quantitative analysis of FDG-CLI signals from iBAT between high and high and low endogenous UCP1 level group. Data represent mean ± SD (n = 5 per group). ns, not significant.

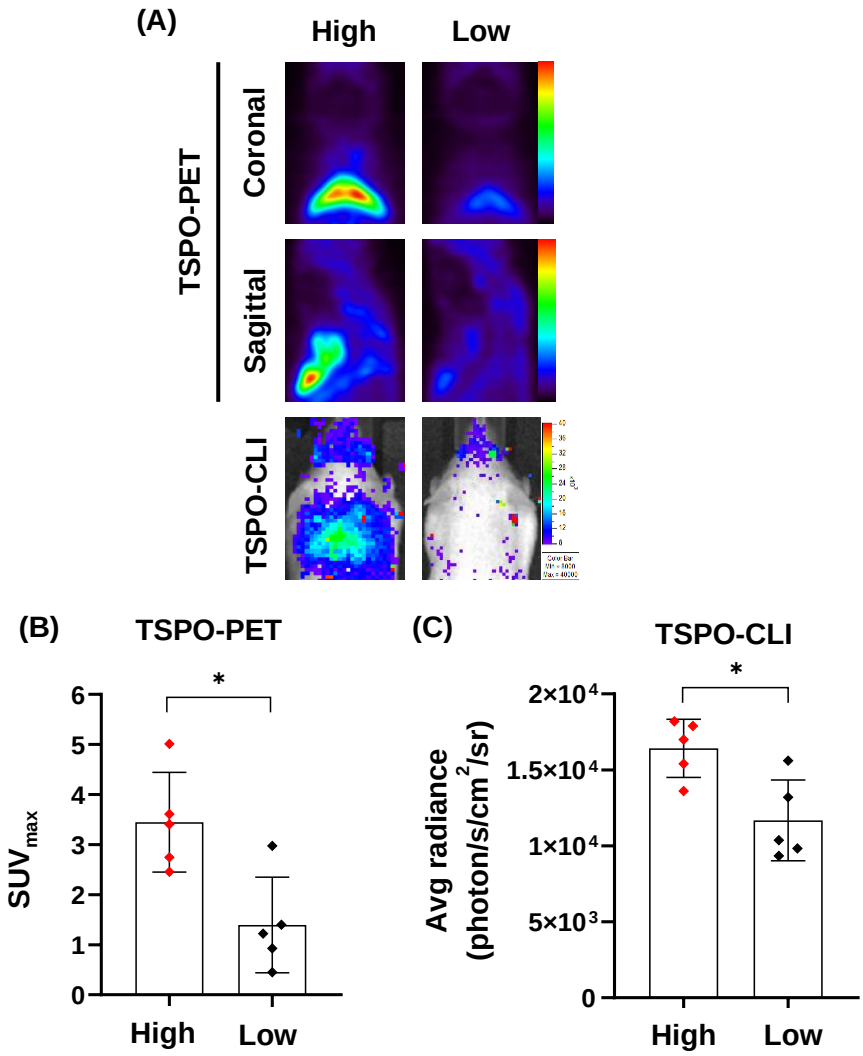

Figure 1-10. TSPO-PET and TSPO-CLI between high and low UCP1 level group. (A) Representative TSPO-PET and TSPO-CLI images between high and low endogenous UCP1 level group. (B) Quantitative analysis of TSPO-PET signals from iBAT between high and low endogenous UCP1 level group. (C) Quantitative analysis of TSPO-CLI signals from iBAT between high and low endogenous UCP1 level group. Data represent mean ± SD (n = 5 per group). $^{*}P < 0.05$.

High molar activity as essential factor for obtaining TSPO-CLI as well as TPSO-PET on iBAT imaging in UCP1 reporter mouse

Molar activity (A_m, commonly known as "specific activity") is defined as the ratio of radioactivity per mole of precursor measured in Becquerel per mole (Bq/mol, or GBq/μmol). High A_m results in a better quality of nuclear medicine images and analysis due to fewer non-labeled precursors and less competition with labeled radioactive compounds. Since I revealed that TSPO is superior to [^{18}F]FDG in obtaining iBAT-specific images, I used [^{18}F]fm-PBR28-d_2 with different A_m to investigate the conditions for obtaining better TSPO-PET and TSPO-CLI. As shown in **Figure 1-11A**, TSPO-PET with high A_m (HA_m, more than 2,349.8 GBq/μmol) of [^{18}F]fm-PBR28-d_2 showed clearly PET signals from iBAT. Consistent with TSPO-PET imaging, TSPO-CLI with HA_m of [^{18}F]fm-PBR28-d_2 was obtained with the superior image quality of iBAT. On the other hand, TSPO-PET with low A_m (LA_m, less than 172.5 GBq/μmol) of [^{18}F]fm-PBR28-d_2 showed poor PET signals from iBAT. Furthermore, TSPO-CLI with LA_m of [^{18}F]fm-PBR28-d_2 was obtained with low image-quality of iBAT (**Figure 1-11B**). Quantitative analysis indicated that SUV_{max} for PET signals of the HA_m group was 4.06-fold higher than the LA_m group (HA_m *vs.* LA_m, 14.27 ± 3.28 *vs.* 3.51 ± 0.9, $^{****}P < 0.0001$, **Figure 1-11C**), and CLI signals of the HA_m

group were 1.54−fold higher than in the LA_m group (Average radiance, photon/s/cm^2/sr, HA_m *vs.* LA_m 16,328.57 ± 5,781.78 *vs.* 10,632.86 ± 1,864.58, $^*P = 0.04$, **Figure 1−11D**).

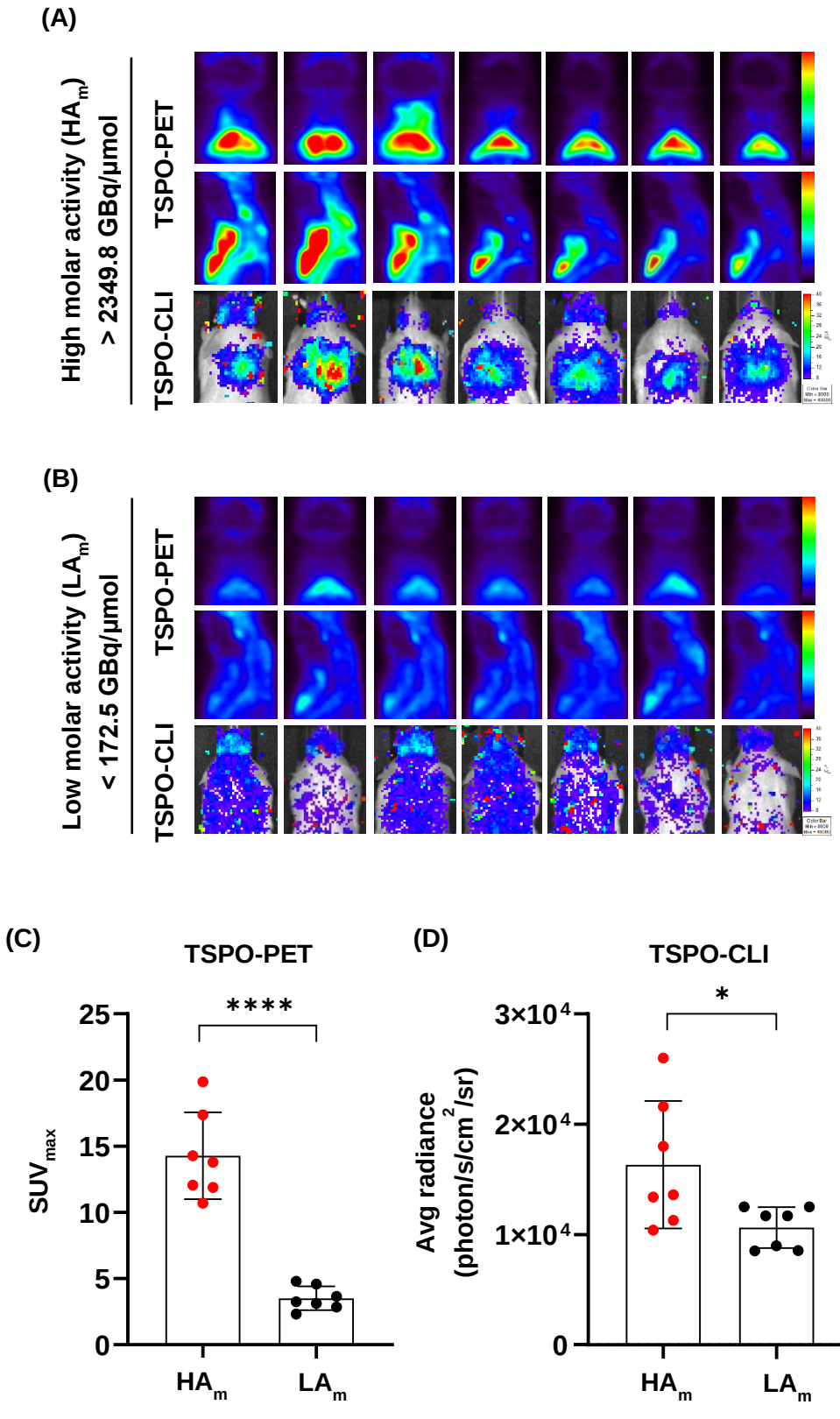
(A)
High molar activity (HAm)
> 2349.8 GBq/μmol
TSPO-PET
TSPO-CLI
(B)
Low molar activity (LAm)
< 172.5 GBq/μmol
TSPO-PET
TSPO-CLI
(C)
TSPO-PET
****
SUVmax
25
20
15
10
5
0
HAm
LAm
(D)
TSPO-CLI
*
Avg radiance
(photon/s/cm2/sr)
3×10⁴
2×10⁴
1×10⁴
0
HAm
LAm

Figure 1-11. TSPO-PET and TSPO-CLI with different molar activity (A_m) for iBAT imaging in UCP1 reporter mouse. (A) TSPO-PET for iBAT imaging with HA_m of [^{18}F]fm-PBR28-d_2. (B) TSPO-CLI for iBAT imaging with LA_m of [^{18}F]fm-PBR28-d_2. (C) Quantitative analysis of PET signals from HA_m or LA_m of [^{18}F]fm-PBR28-d_2. (D) Quantitative analysis of CLI signals from HA_m or LA_m of [^{18}F]fm-PBR28-d_2. Data represent mean ± SD (n = 7 per group). $^{*}P < 0.05$, $^{****}P < 0.001$.

DISCUSSION

The UCP1 reporter mouse is a valuable model to image iBAT as it specifically shows the expression of endogenous UCP1, a biomarker of BAT, by bioluminescence and fluorescence imaging *in vivo* (**Figure 1-2**). UCP1, TSPO and Luciferase expression were correlated in iBAT of UCP1 reporter mouse (**Figure 1-4**). From the biodistribution results of [^{18}F]FDG and [^{18}F]fm-PBR28-d_2, it was observed that [^{18}F]fm-PBR28-d_2 specifically binds to iBAT (**Figure 1-7**). Since [^{18}F]FDG is capable of targeting iBAT, PET and CLI images are limited by changes in glucose metabolism in the body, its high uptake in the brain and heart could interfere with the reliability of [^{18}F]FDG in iBAT images. In addition, iWAT also showed higher binding of [^{18}F]fm-PBR28-d_2 than [^{18}F]FDG, suggesting that browning of iWAT can be effectively observed under specific conditions to be mentioned in chapter 2.

To evaluate which of the [^{18}F]FDG and [^{18}F]fm-PBR28-d_2 better reflected UCP1 expression, two groups (high and low) were divided according to the endogenous level of UCP1. The [^{18}F]fm-PBR28-d_2 uptake was correlated with endogenous levels of UCP1 without uptake in brain and heart. However, [^{18}F]FDG uptake was not

correlated with endogenous levels of UCP1 (**Figure 1-9**). There was no difference between groups according to the endogenous levels of UCP1, and an off-target effect was shown with higher uptake in the brain and heart than in iBAT. That is, [^{18}F]FDG appears to be dispersed and absorbed by other organs with enhanced glucose metabolism independent of endogenous UCP1 levels in iBAT. In particular, when using the [^{18}F]fm-PBR28-d_2, unlike when using [^{18}F]FDG, significant differences were observed according to the endogenous level of UCP1 in CLI and PET. Comprehensively, These data indicated that [^{18}F]fm-PBR28-d_2 was significantly more useful than [^{18}F]FDG for obtaining iBAT images in both PET and CLI.

Since an optimal dose of radionuclide activity is required for an accurate PET scan, the molar activity of an imaging probe A_m, defined as the radioactivity in a specific amount of tracer, is important [61]. In general, receptors with low density in the body require high molar activity because even a small amount of non-radiolabeled compounds can bind to and saturate the target protein, making accurate observation difficult. High A_m is required because even highly toxic molecules such as [^{11}C]carfentanil can produce pharmacological activity [62]. Therefore, higher molar activity is considered to be an important factor not only for PET but also for detection using CCD

cameras in optical equipment such as CLI. However, endogenous molecules labeled with radionuclides on glucose or amino acids, such as [^{18}F]FDG or L-[methyl-^{11}C]methionine, compete with the endogenous compound in blood and tissues. Also for antibodies, administration of [^{111}In]J591 at low A_m with the addition of non-labeled antibody has been reported to advantage retention time and lesion to non-lesion retention time ratio [63]. Therefore, it was necessary to determine the optimal range of molar activity of a probe to obtain high-quality images [64]. In this study, for [^{18}F]fm-PBR28-d_2, a molar activity of at least 2300 GBq/μmol was required to obtain better CLI images as well as PET (**Figure 1-11**). Consistent with other reports, injection of [^{18}F]F-DPA, TSPO-targeting probe with high molar activity, resulted in higher brain binding with lower "self-blocking" [61]. The results using [^{18}F]fm-PBR28-d_2, which has a low molar activity, suggest that the PET and CLI signals may be relatively weak because non-radiolabeled molecules from BAT can competitively bind to TSPO. However, to propose BAT-specific imaging using TSPO, it is necessary to secure objectivity by comparing the imaging results according to A_m of different TSPO targeting probes.

The emission spectrum of CL is UV-weighted, and the intensity decreases at a rate of one square of the wavelength ($1/\lambda^2$). The

intensity of CR depends on the isotope photon yield and activity and decreases rapidly with tissue thickness. To overcome this limitation, cameras such as a highly sensitive charged- coupled device (CCD) and probes are being developed that convert Cerenkov emission wavelengths to red-shift to increase tissue permeability [65, 66]. However, BAT imaging using CLI does not have difficult following reasons: 1) It is separated from the location of large organs; 2) The photons of CR can be easily detected because the BAT location is shallow; 3) It has a triangular shape unique to BAT, so it can be distinguished from other organs [59].

Conclusions

In chapter 1, The correlation between UCP1 and Luciferase expression of BAT in UCP1 reporter mice was demonstrated by Western blotting, IHC and BLI. Based on biochemical data, image and quantitatively analyses, I suggest that TSPO-targeting probe can overcome image interpretation errors caused by the off-target effects of [^{18}F]FDG. CLI using a TSPO-targeting probe is a reliable bioimaging marker for acquiring BAT images along with PET.

CHAPTER 2

The application of TSPO-CLI in BAT imaging under various physiological conditions

INTRODUCTION

2.1. Study Background

Cold stimulation is a representative stimulation method of BAT that promotes and activates glucose uptake by increasing the expression of glucose transporter 4 (GLUT4) and genes involved in glucose metabolism [67]. Cold stimulation releases norepinephrine from the sympathetic nervous system and activates β-adrenergic receptors [68, 69]. Cold stimulation, as mentioned in chapters 1, not only activates BAT but also induces beige or brown-in-white (brite) cells from WAT [70]. These cells, like BAT, show increased fuel oxidation and capacity of thermogenesis and multilocular lipid droplets than WAT after cold stimulation [71]. Cold stimulation also increased mitochondria content including UCP1 expressions and related gene markers for BAT [72]. Cold-induced thermogenic activation of BAT may also induce the expression of nitric oxide synthase in these fat depots, contributing to enhanced blood flow in BAT for increased thermogenesis [73, 74]. In 2009, the function of BAT was first reported in adult humans by PET using [^{18}F]FDG under cold stimulation [75]. In studies before 2009, it has difficult

that the prevalence of BAT using [^{18}F]FDG-PET to analyze due to various temperature environments when subjects performed PET scans [76]. Importantly, 96% of subjects were detected iBAT by [^{18}F]FDG-PET under cold stimulation but less than 10% of subjects were detected under no stimulation or thermoneutral (TN) condition. Therefore, this method may have difficult standardizing the iBAT-specific imaging technique with [^{18}F]FDG-PET to the subjects.

In general, the use of an anesthetic is usually essential for clinical surgical procedures or preclinical small animal imaging to keep the animal motionless for the duration of the scan [77, 78]. An anesthetic commonly used for small animals is an inhalational anesthetic using isoflurane, which is highly lipid solubility and is absorbed into the brain through alveoli into the blood stream [79]. However, continuous inhalation anesthesia with isoflurane during image acquisition in small animals shows hypothermia-like physiological changes that reduce the metabolism of central processes [80, 81]. The mechanism of action with anesthetics has been proposed to act as a potential target of ion channels such as NA^{+}, γ-aminobutyric acid, type A ($GABA_A$), or ligand-gated receptors and channels [82-84]. In particular, when isoflurane binds to the $GABA_A$ receptor binding site, $GABA_A$ receptor-mediated

inhibitory postsynaptic actions (GABAergic) are activated [85, 86]. The effects of isoflurane anesthesia showed changes in the binding of various radioligands on PET neuroimaging. In addition, [^{18}F]flumazenil, a $GABA_A$ receptor antagonist, has been shown to reduce radioligand binding affinity under inhalation anesthesia compared to the awake state [87]. Especially, the binding of [^{11}C]DPA-713, another TSPO radioligand, was shown to decrease with isoflurane exposure time in the monkey brain [88]. However, there are no studies that change PET or optical imaging of BAT by isoflurane anesthesia.

2.2. Purpose of Research

In chapter 2, one of the main aims is to evaluate the activity level using [^{18}F]FDG and [^{18}F]fm-PBR28-d_2, a TSPO-targeting PET probe, under cold exposure that regulates BAT activity. UCP1 reporter mouse were exposed for 4 h to each group of cold stimulation or TN condition. Another main aim is to evaluate BAT activity after prolonged isoflurane anesthesia by PET and CLI using [^{18}F]FDG and [^{18}F]fm-PBR28-d_2. UCP1 reporter mouse was anesthetized with isoflurane for less than 2 h (short-term) or more than 2 h (long-term) before intravenous injection of [^{18}F]FDG and [^{18}F]fm-PBR28-d_2. Finally, the changes in UCP1 expression using

[^{18}F]FDG and [^{18}F]fm−PBR28−d_2 were evaluated by CLI as well as PET by changes in physiological conditions involved in BAT activity.

MATERIALS AND METHODS

1. Acute cold stimulation and thermoneutral conditions

Before injecting [^{18}F]FDG or [^{18}F]fm-PBR28-d_2, UCP1 reporter mice in the cold stimulation group were acclimatized to a space of at about 4℃ for 4 h. During acclimatization, each individual was housed in a separate compartment to prevent them from maintaining body temperature close to each other [89]. On the other hand, UCP1 reporter mice of thermoneutral conditions were acclimatized to at about 30 ℃ using a heating pad for 4 h.

2. Inhalation of anesthesia using isoflurane

UCP1 reporter mice were anesthetized with isoflurane (Troikaa Pharmaceuticals Ltd, Gujarat, India) combined with pure oxygen before injection of [^{18}F]FDG or [^{18}F]fm-PBR28-d_2 and during PET and CLI acquisition. I divided it into two groups based on 2 h from the injection of [^{18}F]FDG or [^{18}F]fm-PBR28-d_2 to the total time that anesthesia was maintained during image acquisition.

RESULTS

[^{18}F]FDG-PET and [^{18}F]FDG-CLI of iBAT in UCP1 reporter mouse under cold exposure and thermoneutral conditions.

As mentioned above, Cold stimulation is one of the representative physiological conditions for activating and obtaining iBAT target images. Therefore, I investigated PET and CLI images using [^{18}F]FDG and [^{18}F]fm-PBR28-d_2 according to iBAT activation under the cold stimulation (cold, 4 ℃) or thermoneutral condition (TN, 30 ℃) in UCP1 reporter mouse. UCP1 reporter mice were exposed to each group of cold or TN for 4 h. Consistent with previous reports, **Figure 2-1A** shows that [^{18}F]FDG-PET of iBAT was higher uptake in the cold exposure group than the TN group. Similarly, TSPO-CLI of iBAT was higher in the cold exposure group than in the TN group (**Figure 2-1B**). Quantitative analysis indicated that TSPO-PET signals from iBAT were 1.53-fold higher in the cold exposure group than TN group (SUV_{max}, cold *vs.* TN, 1.10 ± 0.24 *vs.* 0.72 ± 0.11, $^{*}P = 0.028$, **Figure 2-1C**). Also, TSPO-CLI signals from iBAT were higher 1.18-fold in the cold exposure group than TN group (Average radiance, photon/s/cm^2/sr, cold *vs.* TN, 15,312.5 ± 1,238.02 *vs.* 12,907.5 ± 881.64, $^{*}P = 0.0194$, **Figure 2-1D)**.

(A)

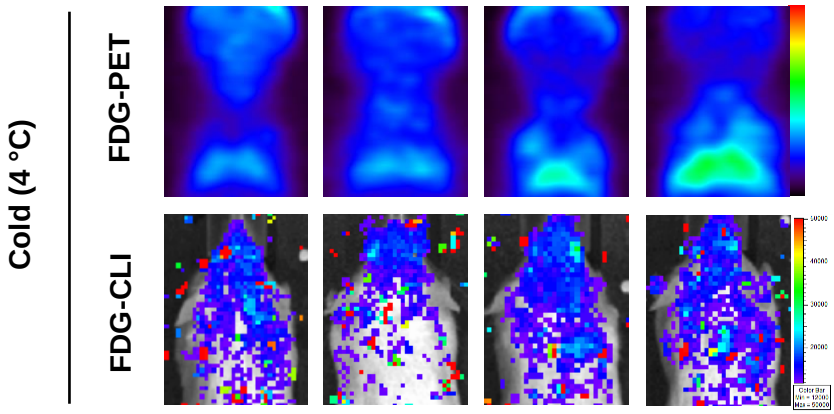
Cold (4 °C)
FDG-PET
FDG-CLI

(B)

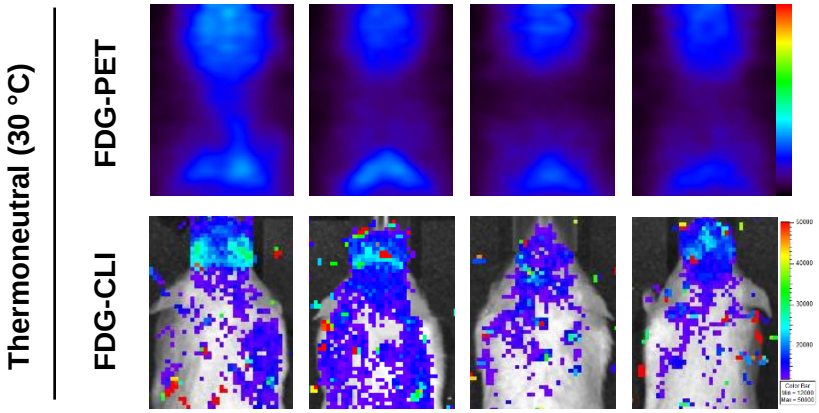
Thermoneutral (30 °C)
FDG-PET
FDG-CLI

(C)

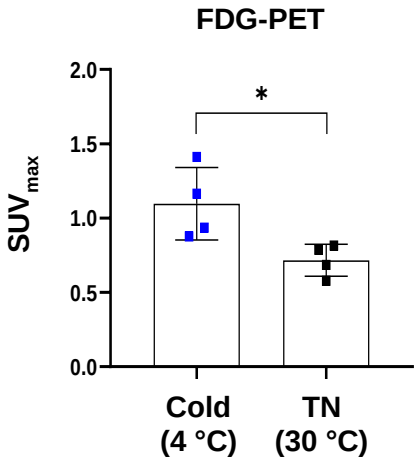
FDG-PET
SUVmax
2.0
1.5
1.0
0.5
0.0
*
Cold
(4 °C)
TN
(30 °C)

(D)

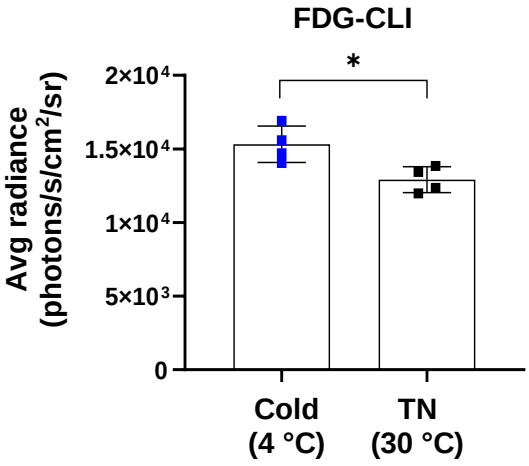
FDG-CLI
Avg radiance
(photons/s/cm2/sr)
2×10⁴
1.5×10⁴
1×10⁴
5×10³
0
*
Cold
(4 °C)
TN
(30 °C)

Figure 2-1. [^{18}F]FDG-PET and [^{18}F]FDG-CLI of iBAT under cold stimulation and TN conditions. (A) [^{18}F]FDG-PET and [^{18}F]FDG-CLI images of iBAT under cold stimulation. (B) [^{18}F]FDG-PET and [^{18}F]FDG-CLI images of iBAT under TN conditions. (C) Quantitative analysis of [^{18}F]FDG-PET SUV_{max} signals from iBAT under cold and TN conditions. (D) Quantitative analysis of [^{18}F]FDG-CLI signals from iBAT under cold and TN conditions. Data represent mean ± SD (n = 4 per group). $^{*}P < 0.05$.

TSPO-PET and TSPO-CLI of iBAT in UCP1 reporter mouse under cold exposure and TN conditions.

Figure 2-2A shows that TSPO-PET of iBAT clearly had higher uptake in the cold stimulation group than the TN group. Similarly, TSPO-CLI of iBAT was higher in the cold exposure group than the TN group (**Figure 2-2B**). Quantitative analysis indicated that TSPO-PET signals from iBAT were 2.45-fold higher in the cold exposure group than TN group (SUV_{max}, cold *vs.* TN, 3.86 ± 0.96 *vs.* 1.57 ± 0.56, $^{**}P = 0.0064$, **Figure 2-2C**). Also, TSPO-CLI signals from iBAT were higher 1.86-fold in the cold exposure group than TN group (Average radiance, photon/s/cm^2/sr, cold *vs.* TN, 15,437.5 ± 4,683.15 *vs.* 8,259.5 ± 2,043.58, $^{*}P = 0.029$, **Figure 2-2D**).

(A)

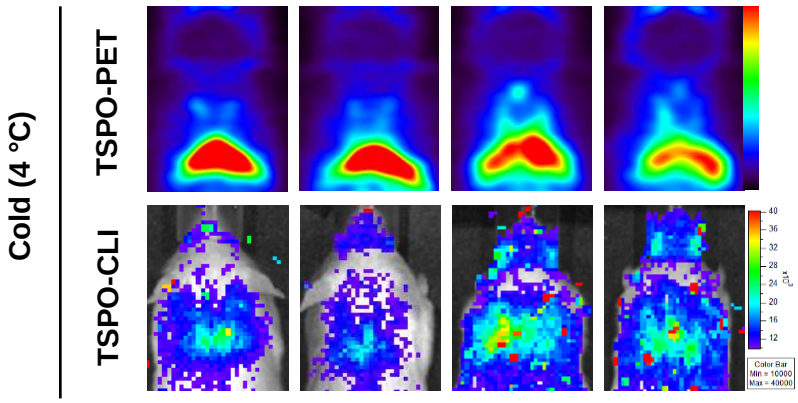
Cold (4 °C)
TSPO-PET
TSPO-CLI
40
36
32
28
24
20
16
12
Color Bar
Min = 10000
Max = 40000

(B)

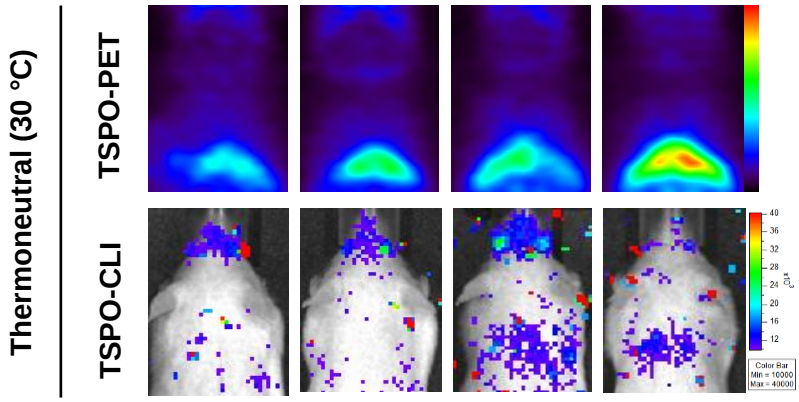
Thermoneutral (30 °C)
TSPO-PET
TSPO-CLI
40
36
32
28
24
20
16
12
Color Bar
Min = 10000
Max = 40000

(C)

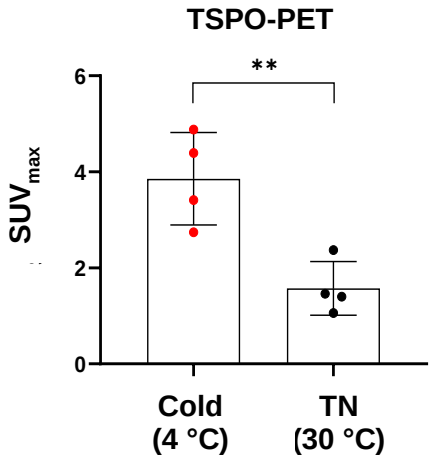
TSPO-PET
**
SUVmax
6
4
2
0
Cold
(4 °C)
TN
(30 °C)

(D)

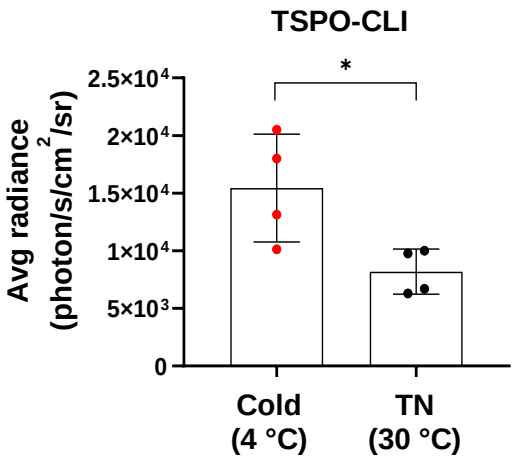
TSPO-CLI
*
Avg radiance
(photon/s/cm2/sr)
2.5×10⁴
2×10⁴
1.5×10⁴
1×10⁴
5×10³
0
Cold
(4 °C)
TN
(30 °C)

Figure 2-2. TSPO-PET and TSPO-CLI of iBAT under cold exposure and TN conditions. (A) TSPO-PET and TSPO-CLI images of iBAT under cold stimulation conditions. (B) TSPO-PET and TSPO-CLI images of iBAT under TN conditions. (C) Quantitative analysis of TSPO-PET SUV_{max} signals from iBAT under cold and TN conditions. (D) Quantitative analysis of TSPO-CLI signals from iBAT under cold and TN conditions. Data represent mean ± SD (n = 4 per group). $^{*}P < 0.05$, $^{**}P < 0.01$.

Monitoring of [^{18}F]FDG-PET and [^{18}F]FDG-CLI of iBAT under isoflurane anesthesia dependent on time in UCP1 reporter mouse

As another physiological condition, PET and CLI of iBAT were investigated using [^{18}F]FDG and TSPO-targeting probe according to anesthesia conditions essential for preclinical imaging or clinical surgery. I examined PET and CLI of iBAT using [^{18}F]FDG and TSPO-targeting probe by dividing the anesthesia time into short and long groups. To investigate the difference in iBAT imaging according to isoflurane anesthesia time, I designated the group with an anesthetic time of less than 2 h as the short-term group and the group with an anesthesia time of more than 2 h as the long-term group. As shown in **Figure 2-3A, 3B**, it was difficult to observe a significant difference between the short-term group and long-term group anesthesia groups for both [^{18}F]FDG-PET and [^{18}F]FDG-CLI. Furthermore, quantitative analysis of both [^{18}F]FDG-PET (**Figure 2-3C**) and [^{18}F]FDG-CLI (**Figure 2-3D**) signal were no significant difference.

(A)

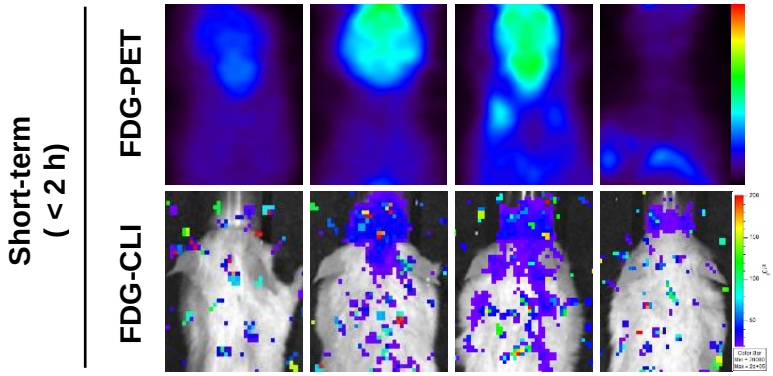
Short-term
(< 2 h)
FDG-PET
FDG-CLI

(B)

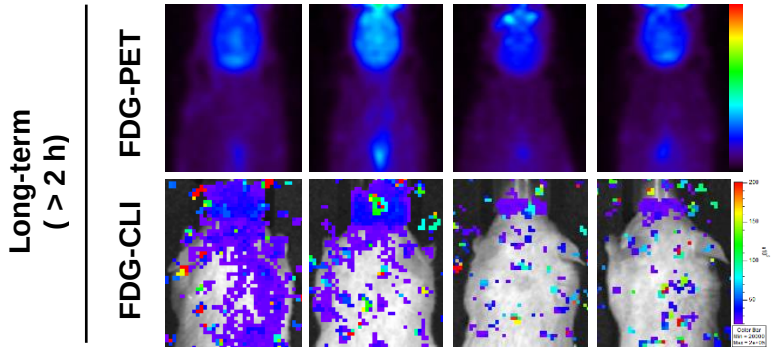
Long-term
(> 2 h)
FDG-PET
FDG-CLI

(C)

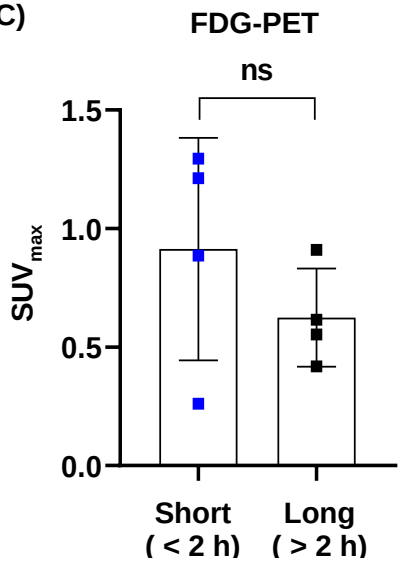
FDG-PET
ns
1.5
1.0
0.5
0.0
SUVmax
Short
(< 2 h)
Long
(> 2 h)

(D)

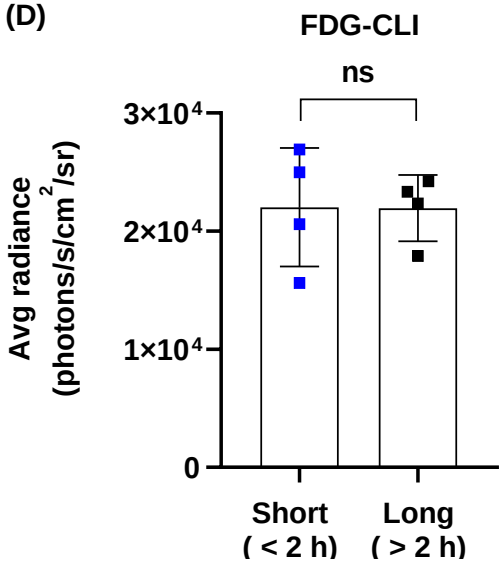
FDG-CLI
ns
3×10⁴
2×10⁴
1×10⁴
0
Avg radiance
(photons/s/cm²/sr)
Short
(< 2 h)
Long
(> 2 h)

Figure 2-3. [^{18}F]FDG-PET and [^{18}F]FDG-CLI of iBAT imaging under isoflurane anesthesia dependent on time. (A) [^{18}F]FDG-PET and [^{18}F]FDG-CLI images under short exposure of isoflurane anesthesia. (B) [^{18}F]FDG-PET and [^{18}F]FDG-CLI images under long exposure of isoflurane anesthesia. (C) Quantitative analysis of PET signals from iBAT with [^{18}F]FDG under short or long exposure isoflurane anesthesia. (D) Quantitative analysis of CLI signals from iBAT with [^{18}F]FDG under short or long exposure isoflurane anesthesia. Data represent mean ± SD (n = 4 per group). ns, not significant.

Monitoring of TSPO-PET and TSPO-CLI of iBAT under isoflurane anesthesia dependent on time in UCP1 reporter mouse

Interestingly, TSPO-PET and TSPO-CLI signals in [^{18}F]fm-PBR28-d_2 from iBAT were clearly observed under the short-term isoflurane anesthesia group as seen in **Figure 2-4A**. Conversely, both TSPO-PET and TSPO-CLI signals of iBAT were decreased in the long-term isoflurane anesthesia group than short-term isoflurane anesthesia group (**Figure 2-4B**). Quantitative analysis of TSPO-PET signals in iBAT was much higher in the short-term group (3.3-fold) than long-term group (SUV_{max}, short-term *vs.* long-term, 5.387 ± 2.989 *vs.* 1.613 ± 0.699, $^{**}P = 0.0069$, **Figure 15-C**). Consistent with **Figure 2-4C** result, TSPO-CLI signals in iBAT were significantly higher in the short-term group (1.41-fold) than long-term group (Average radiance, photon/s/cm^2/sr, short-term *vs.* long-term, 609,857.1 ± 134,265 *vs.* 429,857.1 ± 97,484.1, $^{*}P = 0.0141$, **Figure 2-4D**).

(A)

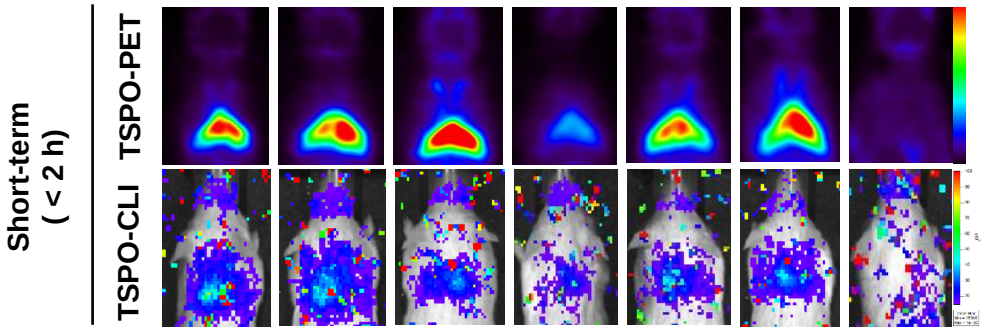
Short-term
(< 2 h)
TSPO-PET
TSPO-CLI

(B)

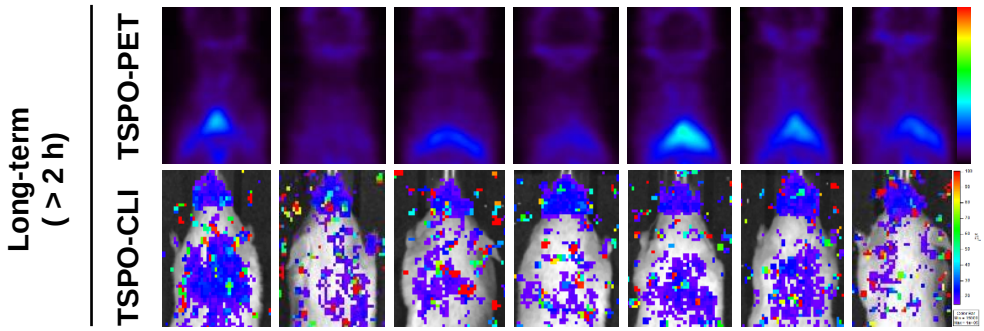
Long-term
(> 2 h)
TSPO-PET
TSPO-CLI

(C)

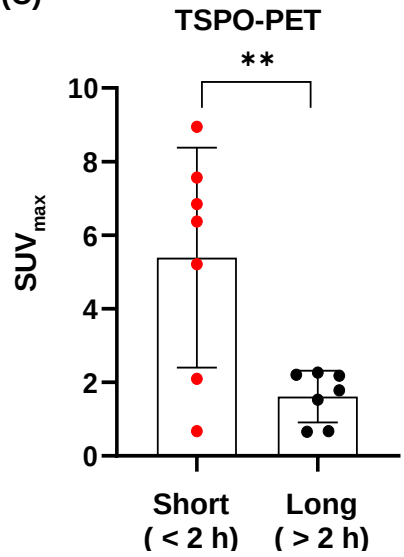
TSPO-PET
**
SUVmax
10
8
6
4
2
0
Short
(< 2 h)
Long
(> 2 h)

(D)

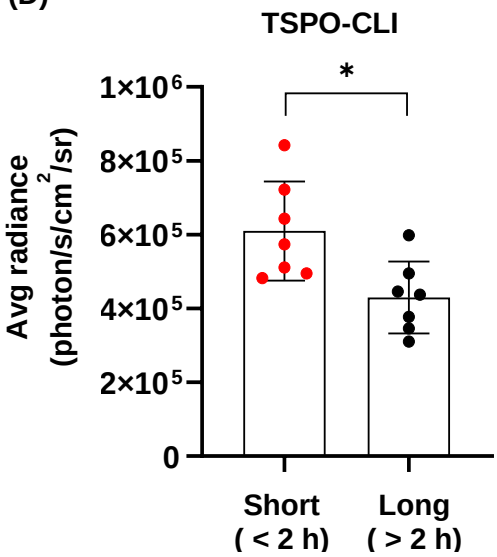
TSPO-CLI
*
Avg radiance
(photon/s/cm2/sr)
1×10^6
8×10^5
6×10^5
4×10^5
2×10^5
0
Short
(< 2 h)
Long
(> 2 h)

Figure 2-4. TSPO-PET and TSPO-CLI of iBAT imaging under isoflurane anesthesia dependent on time. (A) TSPO-PET and TSPO-CLI images under short exposure of isoflurane anesthesia. (B) TSPO-PET and TSPO-CLI images under short exposure of isoflurane anesthesia. (C) Quantitative analysis of PET signals from iBAT with [^{18}F]fm-PBR28-d_2 under short or long exposure isoflurane anesthesia. (D) Quantitative analysis of CLI signals from iBAT with [^{18}F]fm-PBR28-d_2 under short or long exposure isoflurane anesthesia. Data represent mean ± SD (n = 7 per group). $^{*}P < 0.05$, $^{**}P < 0.01$

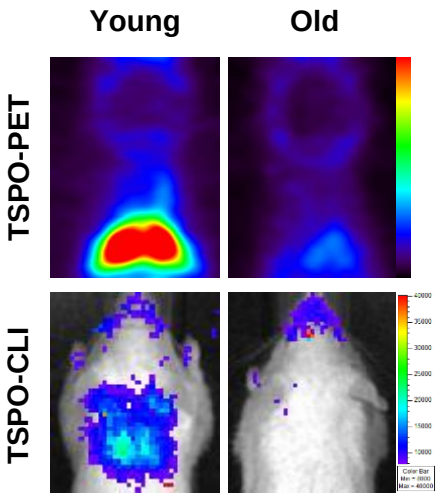

Figure 2-5. TSPO-PET and TSPO-CLI with different date of birth (D.O.B.) in UCP1 reporter mouse.

DISCUSSION

From 2003 to 2012, since the detection rate of iBAT in [^{18}F]FDG-PET is less than 10% in human but cold stimulation increases the image detection rate of iBAT for 33~100% [76]. As mentioned above, UCP1 expression increases in iBAT that uncouples the respiratory chain from oxidative phosphorylation resulting high rate of oxidation and capable of using metabolic energy expenditure to provide heat under cold stimulation [19, 20]. In iBAT with [^{18}F]fm-PBR28-d_2, the TSPO-PET and TSPO-CLI of signals were significantly higher in the cold stimulation group than in the TN group. (**Figure 2-2**). I also evaluated the correlation between UCP1 expression and [^{18}F]FDG uptake in iBAT under cold stimulation conditions but brain uptake was still high (**Figure 2-1**). These results suggest that more sensitive and specific iBAT imaging is possible using TSPO-targeting probe than [^{18}F]FDG.

General anesthesia plays an important role in the long-term PET imaging in the preclinical or patient surgery in the clinic and is also essential in animal studies [90]. The mechanism of action by which inhalational anesthesia in the brain can reduce radioligand

binding is well understood [91, 92]. However, a mechanism related to inhalational anesthesia and the decrease in TSPO radioligand binding affinity has not been elucidated. **Figure 2-4** represent two possible mechanisms related to inhalation anesthesia and TSPO radioligand binding affinity. First, effects of anesthetics on mitochondrial metabolism have been extensively studied, suggesting that anesthesia has a detrimental effect on mitochondrial function [93]. Isoflurane activates the mitochondrial pathway of apoptosis by inducing reactive oxygen species (ROS), promote pro-apoptotic protein including B-cell lymphoma 2 (Bcl-2)-associated X (BAX) levels, and inhibiting anti-apoptotic protein, Bcl-2 family proteins reflecting anti-apoptosis [94]. TSPO mediates cell death and growth as one of the mitochondria permeability transition pore (MPTP) proteins [95]. As mentioned above, because BAT is rich in mitochondria, it is thought that isoflurane may affect TSPO present in mitochondria. Indeed, I observed that the binding of [^{18}F]fm-PBR28-d_2 in PET and CLI was decreased in the group with longer exposure to anesthesia than with shorter exposure (**Figure 2-4**). On the other hand, UCP1 expression and [^{18}F]FDG uptake in iBAT of UCP1 reporter mouse did not change even after long-term isoflurane exposure compared to short-term exposure (**Figure 2-3**). These data indicate that anesthetics can inhibit TSPO expression or function

by reducing mitochondrial metabolic function, excluding factors related to [^{18}F]FDG uptake, and consequently affect iBAT imaging. Therefore, it is necessary to evaluate TSPO expression by obtaining BAT resected from individuals in each group. However, iBAT images using [^{18}F]fm-PBR28-d_2 are generally acquired within 1 h and may not be influenced by the long-term anesthesia effect. Second, TSPO mediates the synthesis of allopregnanolone, a neurosteroids that activates the allosteric $GABA_A$ receptor by transporting cholesterol from the outer mitochondrial membrane to the inner membrane [36]. When mitochondrial function and metabolism are impaired by isoflurane, TSPO-mediated reduction in neurosteroids production that binds to $GABA_A$ receptors cannot be established because it reduces GABAergic. However, when isoflurane binds to $GABA_A$ receptors and activates GABAergic system, it induces hypothermia and slows blood circulation [81]. Therefore, longer than shorter exposure times are expected to lead to reduced pharmacokinetics to reach receptor-ligand binding affinity due to the slowing of blood flow.

In addition to the results of my research in this paper, various iBAT studies are possible in UCP1 reporter mouse using [^{18}F]FDG-PET or [^{18}F]fm-PBR28-d_2. The iBAT images obtained from human [^{18}F]FDG-PET showed decreased glucose uptake with age due to

mitochondrial dysfunction and impairment of endocrine signaling, suggesting that TSPO-PET may also be affected by age [96-98]. Preliminary data showed that younger UCP1 reporter mouse (9 weeks old, n = 1) had higher signals than older UCP1 reporter mouse (36 weeks old, n = 1) under normal conditions in both TSPO-PET and TSPO-CLI. (**Figure 2-5**). However, experiments with adding individuals are needed to explain this observation. Also, since most obese people have white fat as adipocytes, research on obesity treatment through the browning of white fat is of interest. It is well established that diet-induced obese (DIO) mouse models or obese humans have larger adipocytes, fewer mitochondria, and lower UCP1 expression than lean mice or humans [99]. Therefore, iBAT images with UCP1 and TSPO-targeting ligands in the DIO model of UCP1 reporter mice are expected to provide various information on the browning of WAT.

Conclusions

Following Chapter 1, Chapter 2 compared PET and CLI images using FDG and TSPO under various physiological conditions that change the activity of BAT. In the classical cold acclimation method, both [^{18}F]FDG and [^{18}F]fm-PBR28-d_2 showed higher signals from BAT in the cold exposure group than in the TN condition group, but TSPO reflected the signal more sensitively without an off-target effect. Unlike [^{18}F]FDG-PET/CLI data, TSPO-PET and TSPO-CLI signals in iBAT decreased more in the long-term anesthesia group than in the short-term anesthesia group due to mitochondrial damage.

Bibliography

1. Loos RJF, Yeo GSH. The genetics of obesity: from discovery to biology. Nat Rev Genet. 2022; 23: 120–33.
2. Locke AE, Kahali B, Berndt SI, Justice AE, Pers TH, Day FR, et al. Genetic studies of body mass index yield new insights for obesity biology. Nature. 2015; 518: 197–206.
3. González–Muniesa P, Mártinez–González MA, Hu FB, Després JP, Matsuzawa Y, Loos RJF, et al. Obesity. Nat Rev Dis Primers. 2017; 3: 17034.
4. Fang H, Berg E, Cheng X, Shen W. How to best assess abdominal obesity. Curr Opin Clin Nutr Metab Care. 2018; 21: 360–5.
5. Dennison EM, Sayer AA, Cooper C. Epidemiology of sarcopenia and insight into possible therapeutic targets. Nat Rev Rheumatol. 2017; 13: 340–7.
6. Goldenberg L, Saliba W, Hayeq H, Hasadia R, Zeina AR. The impact of abdominal fat on abdominal aorta calcification measured on non–enhanced CT. Medicine (Baltimore). 2018; 97: e13233
7. Kaneda H, Nakajima T, Haruyama A, Shibasaki I, Hasegawa T, Sawaguchi T, et al. Association of serum concentrations of

irisin and the adipokines adiponectin and leptin with epicardial fat in cardiovascular surgery patients. PLoS One. 2018; 13: e0201499.

8. Connelly TM, Juza RM, Sangster W, Sehgal R, Tappouni RF, Messaris E. Volumetric fat ratio and not body mass index is predictive of ileocolectomy outcomes in Crohn's disease patients. Dig Surg. 2014; 31: 219-24.
9. Cypess AM. Reassessing Human Adipose Tissue. N Engl J Med. 2022; 386: 768-79.
10. Sanchez-Gurmaches J, Hung CM, Guertin DA. Emerging Complexities in Adipocyte Origins and Identity. Trends Cell Biol. 2016; 26: 313-26.
11. Wang W, Seale P. Control of brown and beige fat development. Nat Rev Mol Cell Biol. 2016; 17: 691-702.
12. Frankl J, Sherwood A, Clegg DJ, Scherer PE, Öz OK. Imaging Metabolically Active Fat: A Literature Review and Mechanistic Insights. Int J Mol Sci. 2019; 20.
13. van der Lans AA, Vosselman MJ, Hanssen MJ, Brans B, van Marken Lichtenbelt WD. Supraclavicular skin temperature and BAT activity in lean healthy adults. J Physiol Sci. 2016; 66: 77-83.
14. Mirbolooki MR, Constantinescu CC, Pan ML, Mukherjee J.

Quantitative assessment of brown adipose tissue metabolic activity and volume using 18F-FDG PET/CT and β3-adrenergic receptor activation. EJNMMI Res. 2011; 1: 30.

15. Trayhurn P. Brown Adipose Tissue: A Short Historical Perspective. Methods Mol Biol. 2022; 2448: 1-18.
16. Trayhurn P. Origins and early development of the concept that brown adipose tissue thermogenesis is linked to energy balance and obesity. Biochimie. 2017; 134: 62-70.
17. Trayhurn P. Brown Adipose Tissue-A Therapeutic Target in Obesity? Front Physiol. 2018; 9: 1672.
18. Betz MJ, Enerbäck S. Targeting thermogenesis in brown fat and muscle to treat obesity and metabolic disease. Nat Rev Endocrinol. 2018; 14: 77-87.
19. Villarroya F, Cereijo R, Villarroya J, Giralt M. Brown adipose tissue as a secretory organ. Nat Rev Endocrinol. 2017; 13: 26-35.
20. Virtanen KA, Lidell ME, Orava J, Heglind M, Westergren R, Niemi T, et al. Functional brown adipose tissue in healthy adults. N Engl J Med. 2009; 360: 1518-25.
21. Cypess AM, Lehman S, Williams G, Tal I, Rodman D, Goldfine AB, et al. Identification and importance of brown adipose tissue in adult humans. N Engl J Med. 2009; 360: 1509-17.

22. Zingaretti MC, Crosta F, Vitali A, Guerrieri M, Frontini A, Cannon B, et al. The presence of UCP1 demonstrates that metabolically active adipose tissue in the neck of adult humans truly represents brown adipose tissue. Faseb j. 2009; 23: 3113-20.
23. Rahman WT, Wale DJ, Viglianti BL, Townsend DM, Manganaro MS, Gross MD, et al. The impact of infection and inflammation in oncologic [^{18}]F-FDG PET/CT imaging. Biomed Pharmacother. 2019; 117: 109168.
24. Miele E, Spinelli GP, Tomao F, Zullo A, De Marinis F, Pasciuti G, et al. Positron Emission Tomography (PET) radiotracers in oncology--utility of ^{18}F-Fluoro-deoxy-glucose (FDG)-PET in the management of patients with non-small-cell lung cancer (NSCLC). J Exp Clin Cancer Res. 2008; 27: 52
25. Mathupala SP, Ko YH, Pedersen PL. Hexokinase II: cancer's double-edged sword acting as both facilitator and gatekeeper of malignancy when bound to mitochondria. Oncogene. 2006; 25: 4777-86.
26. Gerngroß C, Schretter J, Klingenspor M, Schwaiger M, Fromme T. Active Brown Fat During [^{18}]F-FDG PET/CT Imaging Defines a Patient Group with Characteristic Traits and an Increased Probability of Brown Fat Redetection. J Nucl

Med. 2017; 58: 1104-10.

27. Blondin DP, Labbé SM, Phoenix S, Guérin B, Turcotte É E, Richard D, et al. Contributions of white and brown adipose tissues and skeletal muscles to acute cold-induced metabolic responses in healthy men. J Physiol. 2015; 593: 701-14.

28. Krauss S, Zhang CY, Lowell BB. The mitochondrial uncoupling-protein homologues. Nat Rev Mol Cell Biol. 2005; 6: 248-61.

29. Kozak LP, Anunciado-Koza R. UCP1: its involvement and utility in obesity. Int J Obes (Lond). 2008; 32 Suppl 7: S32-8.

30. Chouchani ET, Kazak L, Spiegelman BM. New Advances in Adaptive Thermogenesis: UCP1 and Beyond. Cell Metab. 2019; 29: 27-37.

31. Brondani LA, Assmann TS, Duarte GC, Gross JL, Canani LH, Crispim D. The role of the uncoupling protein 1 (UCP1) on the development of obesity and type 2 diabetes mellitus. Arq Bras Endocrinol Metabol. 2012; 56: 215-25.

32. Harms M, Seale P. Brown and beige fat: development, function and therapeutic potential. Nat Med. 2013; 19: 1252-63.

33. Kajimura S. Adipose tissue in 2016: Advances in the understanding of adipose tissue biology. Nat Rev Endocrinol.

2017; 13: 69–70.

34. Galmozzi A, Sonne SB, Altshuler-Keylin S, Hasegawa Y, Shinoda K, Luijten IHN, et al. ThermoMouse: an *in vivo* model to identify modulators of UCP1 expression in brown adipose tissue. Cell Rep. 2014; 9: 1584–93.

35. Qiu Y, Sun Y, Xu D, Yang Y, Liu X, Wei Y, et al. Screening of FDA-approved drugs identifies sutent as a modulator of UCP1 expression in brown adipose tissue. EBioMedicine. 2018; 37: 344–55.

36. Rupprecht R, Papadopoulos V, Rammes G, Baghai TC, Fan J, Akula N, et al. Translocator protein (18 kDa) (TSPO) as a therapeutic target for neurological and psychiatric disorders. Nat Rev Drug Discov. 2010; 9: 971–88.

37. Hatori A, Yui J, Yamasaki T, Xie L, Kumata K, Fujinaga M, et al. PET imaging of lung inflammation with [^{18}F]FEDAC, a radioligand for translocator protein (18 kDa). PLoS One. 2012; 7: e45065.

38. Yao R, Pan R, Shang C, Li X, Cheng J, Xu J, et al. Translocator Protein 18 kDa (TSPO) Deficiency Inhibits Microglial Activation and Impairs Mitochondrial Function. Front Pharmacol. 2020; 11: 986.

39. Winkeler A, Boisgard R, Awde AR, Dubois A, Thézé B, Zheng

J, et al. The translocator protein ligand [^{18}F]DPA-714 images glioma and activated microglia *in vivo*. Eur J Nucl Med Mol Imaging. 2012; 39: 811-23.

40. Werry EL, Barron ML, Kassiou M. TSPO as a target for glioblastoma therapeutics. Biochem Soc Trans. 2015; 43: 531-6.
41. Unterrainer M, Mahler C, Vomacka L, Lindner S, Havla J, Brendel M, et al. TSPO PET with [^{18}F]GE-180 sensitively detects focal neuroinflammation in patients with relapsing-remitting multiple sclerosis. Eur J Nucl Med Mol Imaging. 2018; 45: 1423-31.
42. Owen DR, Howell OW, Tang SP, Wells LA, Bennacef I, Bergstrom M, et al. Two binding sites for [^{3}H]PBR28 in human brain: implications for TSPO PET imaging of neuroinflammation. J Cereb Blood Flow Metab. 2010; 30: 1608-18.
43. Ching AS, Kuhnast B, Damont A, Roeda D, Tavitian B, Dollé F. Current paradigm of the 18-kDa translocator protein (TSPO) as a molecular target for PET imaging in neuroinflammation and neurodegenerative diseases. Insights Imaging. 2012; 3: 111-9.
44. Yang J, Yang J, Wang L, Moore A, Liang SH, Ran C.

Synthesis-free PET imaging of brown adipose tissue and TSPO via combination of disulfiram and $^{64}CuCl_2$. Sci Rep. 2017; 7: 8298.

45. Selvaraj V, Tu LN. Current status and future perspectives: TSPO in steroid neuroendocrinology. J Endocrinol. 2016; 231: R1-r30.

46. Hartimath SV, Khanapur S, Boominathan R, Jiang L, Cheng P, Yong FF, et al. Imaging adipose tissue browning using the TSPO-18kDa tracer [(18)F]FEPPA. Mol Metab. 2019; 25: 154-8.

47. Oh C, Song IH, Lee W, Jeon M, Choi J, Baek S, et al. Brown adipose tissue imaging using the TSPO tracer [^{18}F]fluoromethyl-PBR28-d_2: A comparison with [^{18}F]FDG. Nucl Med Biol. 2020; 90-91: 98-103.

48. Ran C, Albrecht DS, Bredella MA, Yang J, Yang J, Liang SH, et al. PET Imaging of Human Brown Adipose Tissue with the TSPO Tracer [^{11}C]PBR28. Mol Imaging Biol. 2018; 20: 188-93.

49. Moon BS, Jung JH, Park HS, Contino M, Denora N, Lee BC, et al. Preclinical comparison study between [^{18}F]fluoromethyl-PBR28 and its deuterated analog in a rat model of neuroinflammation. Bioorg Med Chem Lett. 2018; 28: 2925-

9.

50. Hricak H, Abdel-Wahab M, Atun R, Lette MM, Paez D, Brink JA, et al. Medical imaging and nuclear medicine: a Lancet Oncology Commission. Lancet Oncol. 2021; 22: e136-e72.

51. Robertson R, Germanos MS, Li C, Mitchell GS, Cherry SR, Silva MD. Optical imaging of Cerenkov light generation from positron-emitting radiotracers. Phys Med Biol. 2009; 54: N355-65.

52. Spinelli AE, D'Ambrosio D, Calderan L, Marengo M, Sbarbati A, Boschi F. Cerenkov radiation allows *in vivo* optical imaging of positron emitting radiotracers. Phys Med Biol. 2010; 55: 483-95.

53. Jacques SL. Optical properties of biological tissues: a review. Phys Med Biol. 2013; 58: R37-61.

54. Ruggiero A, Holland JP, Lewis JS, Grimm J. Cerenkov luminescence imaging of medical isotopes. J Nucl Med. 2010; 51: 1123-30.

55. Desvaux E, Courteau A, Bellaye PS, Guillemin M, Drouet C, Walker P, et al. Cherenkov luminescence imaging is a fast and relevant preclinical tool to assess tumour hypoxia *in vivo*. EJNMMI Res. 2018; 8: 111.

56. Zhang Z, Qu Y, Cao Y, Shi X, Guo H, Zhang X, et al. A novel *in*

vivo Cerenkov luminescence image-guided surgery on primary and metastatic colorectal cancer. J Biophotonics. 2020; 13: e201960152.

57. Liu H, Carpenter CM, Jiang H, Pratx G, Sun C, Buchin MP, et al. Intraoperative imaging of tumors using Cerenkov luminescence endoscopy: a feasibility experimental study. J Nucl Med. 2012; 53: 1579-84.

58. Pratt EC, Skubal M, Mc Larney B, Causa-Andrieu P, Das S, Sawan P, et al. Prospective testing of clinical Cerenkov luminescence imaging against standard-of-care nuclear imaging for tumour location. Nat Biomed Eng. 2022; 6: 559-68.

59. Zhang X, Kuo C, Moore A, Ran C. *In vivo* optical imaging of interscapular brown adipose tissue with ^{18}F-FDG via Cerenkov luminescence imaging. PLoS One. 2013; 8: e62007.

60. Zhang X, Kuo C, Moore A, Ran C. Cerenkov luminescence imaging of interscapular brown adipose tissue. J Vis Exp. 2014: e51790.

61. Keller T, López-Picón FR, Krzyczmonik A, Forsback S, Takkinen JS, Rajander J, et al. Comparison of high and low molar activity TSPO tracer [^{18}F]F-DPA in a mouse model of Alzheimer's disease. J Cereb Blood Flow Metab. 2020; 40:

1012–20.

62. Perkins G, Sheth R, Greguric I, Pascali G. Optimisation of [^{11}C]Raclopride production using a Synthra GPextent system. Curr Radiopharm. 2014; 7: 100–6.

63. Luurtsema G, Pichler V, Bongarzone S, Seimbille Y, Elsinga P, Gee A, et al. EANM guideline for harmonisation on molar activity or specific activity of radiopharmaceuticals: impact on safety and imaging quality. EJNMMI Radiopharm Chem. 2021; 6: 34.

64. Wurzer A, Pollmann J, Schmidt A, Reich D, Wester HJ, Notni J. Molar Activity of Ga–68 Labeled PSMA Inhibitor Conjugates Determines PET Imaging Results. Mol Pharm. 2018; 15: 4296–302.

65. Luurtsema G, Pichler V, Bongarzone S, Seimbille Y, Elsinga P, Gee A, et al. EANM guideline for harmonisation on molar activity or specific activity of radiopharmaceuticals: impact on safety and imaging quality. EJNMMI Radiopharm Chem. 2021; 6: 34.

66. Bernhard Y, Collin B, Decréau RA. Redshifted Cherenkov Radiation for *in vivo* Imaging: Coupling Cherenkov Radiation Energy Transfer to multiple Förster Resonance Energy Transfers. Sci Rep. 2017; 7: 45063.

67. Lee P, Bova R, Schofield L, Bryant W, Dieckmann W, Slattery A, et al. Brown Adipose Tissue Exhibits a Glucose-Responsive Thermogenic Biorhythm in Humans. Cell Metab. 2016; 23: 602-9.

68. Razzoli M, Emmett MJ, Lazar MA, Bartolomucci A. β-Adrenergic receptors control brown adipose UCP-1 tone and cold response without affecting its circadian rhythmicity. Faseb j. 2018; 32: 5640-6.

69. Bachman ES, Dhillon H, Zhang CY, Cinti S, Bianco AC, Kobilka BK, et al. betaAR signaling required for diet-induced thermogenesis and obesity resistance. Science. 2002; 297: 843-5.

70. Cereijo R, Giralt M, Villarroya F. Thermogenic brown and beige/brite adipogenesis in humans. Ann Med. 2015; 47: 169-77.

71. Wu J, Cohen P, Spiegelman BM. Adaptive thermogenesis in adipocytes: is beige the new brown? Genes Dev. 2013; 27: 234-50.

72. Sepa-Kishi DM, Jani S, Da Eira D, Ceddia RB. Cold acclimation enhances UCP1 content, lipolysis, and triacylglycerol resynthesis, but not mitochondrial uncoupling and fat oxidation, in rat white adipocytes. Am J Physiol Cell

Physiol. 2019; 316: C365-c76.

73. Wickham KA, Steele SW, Cheung SS. Effects of acute dietary nitrate supplementation on cold-induced vasodilation in healthy males. Eur J Appl Physiol. 2021; 121: 1431-9.

74. Kikuchi-Utsumi K, Gao B, Ohinata H, Hashimoto M, Yamamoto N, Kuroshima A. Enhanced gene expression of endothelial nitric oxide synthase in brown adipose tissue during cold exposure. Am J Physiol Regul Integr Comp Physiol. 2002; 282: R623-6.

75. van Marken Lichtenbelt WD, Vanhommerig JW, Smulders NM, Drossaerts JM, Kemerink GJ, Bouvy ND, et al. Cold-activated brown adipose tissue in healthy men. N Engl J Med. 2009; 360: 1500-8.

76. Bauwens M, Wierts R, van Royen B, Bucerius J, Backes W, Mottaghy F, et al. Molecular imaging of brown adipose tissue in health and disease. Eur J Nucl Med Mol Imaging. 2014; 41: 776-91.

77. Elfving B, Bjørnholm B, Knudsen GM. Interference of anaesthetics with radioligand binding in neuroreceptor studies. Eur J Nucl Med Mol Imaging. 2003; 30: 912-5.

78. Hassoun W, Le Cavorsin M, Ginovart N, Zimmer L, Gualda V, Bonnefoi F, et al. PET study of the [11C]raclopride binding in

the striatum of the awake cat: effects of anaesthetics and role of cerebral blood flow. Eur J Nucl Med Mol Imaging. 2003; 30: 141-8.

79. Satuito M, Tom J. Potent Inhalational Anesthetics for Dentistry. Anesth Prog. 2016; 63: 42-8; quiz 9.

80. Rufiange M, Leung VSY, Simpson K, Pang DSJ. Pre-warming before general anesthesia with isoflurane delays the onset of hypothermia in rats. PLoS One. 2020; 15: e0219722.

81. Shimaoka H, Shiina T, Suzuki H, Horii Y, Horii K, Shimizu Y. Successful induction of deep hypothermia by isoflurane anesthesia and cooling in a non-hibernator, the rat. J Physiol Sci. 2021; 71: 10.

82. Yang E, Granata D, Eckenhoff RG, Carnevale V, Covarrubias M. Propofol inhibits prokaryotic voltage-gated Na^+ channels by promoting activation-coupled inactivation. J Gen Physiol. 2018; 150: 1299-316.

83. Zhou C, Liu J, Chen XD. General anesthesia mediated by effects on ion channels. World J Crit Care Med. 2012; 1: 80-93.

84. Garcia PS, Kolesky SE, Jenkins A. General anesthetic actions on GABA(A) receptors. Curr Neuropharmacol. 2010; 8: 2-9.

85. Jia F, Yue M, Chandra D, Homanics GE, Goldstein PA,

Harrison NL. Isoflurane is a potent modulator of extrasynaptic GABA(A) receptors in the thalamus. J Pharmacol Exp Ther. 2008; 324: 1127-35.

86. Woll KA, Zhou X, Bhanu NV, Garcia BA, Covarrubias M, Miller KW, et al. Identification of binding sites contributing to volatile anesthetic effects on GABA type A receptors. Faseb j. 2018; 32: 4172-89.

87. Palner M, Beinat C, Banister S, Zanderigo F, Park JH, Shen B, et al. Effects of common anesthetic agents on [^{18}F]flumazenil binding to the GABA(A) receptor. EJNMMI Res. 2016; 6: 80.

88. Tsukada H, Nishiyama S, Ohba H, Kanazawa M, Kakiuchi T, Harada N. Comparing amyloid-β deposition, neuroinflammation, glucose metabolism, and mitochondrial complex I activity in brain: a PET study in aged monkeys. Eur J Nucl Med Mol Imaging. 2014; 41: 2127-36.

89. Lim S, Honek J, Xue Y, Seki T, Cao Z, Andersson P, et al. Cold-induced activation of brown adipose tissue and adipose angiogenesis in mice. Nat Protoc. 2012; 7: 606-15.

90. Aksenov DP, Gascoigne DA, Greenberg SB, Minhaj MM. Preclinical and clinical paediatric anaesthesia research. Lancet Child Adolesc Health. 2023; 7: 6-8.

91. Kitano H, Kirsch JR, Hurn PD, Murphy SJ. Inhalational

anesthetics as neuroprotectants or chemical preconditioning agents in ischemic brain. J Cereb Blood Flow Metab. 2007; 27: 1108-28.

92. Campagna JA, Miller KW, Forman SA. Mechanisms of actions of inhaled anesthetics. N Engl J Med. 2003; 348: 2110-24.
93. Jevtovic-Todorovic V, Boscolo A, Sanchez V, Lunardi N. Anesthesia-induced developmental neurodegeneration: the role of neuronal organelles. Front Neurol. 2012; 3: 141.
94. Zhang Y, Dong Y, Wu X, Lu Y, Xu Z, Knapp A, et al. The mitochondrial pathway of anesthetic isoflurane-induced apoptosis. J Biol Chem. 2010; 285: 4025-37.
95. De Marchi E, Bonora M, Giorgi C, Pinton P. The mitochondrial permeability transition pore is a dispensable element for mitochondrial calcium efflux. Cell Calcium. 2014; 56: 1-13.
96. Tajima K, Ikeda K, Chang HY, Chang CH, Yoneshiro T, Oguri Y, et al. Mitochondrial lipoylation integrates age-associated decline in brown fat thermogenesis. Nat Metab. 2019; 1: 886-98.
97. Pfannenberg C, Werner MK, Ripkens S, Stef I, Deckert A, Schmadl M, et al. Impact of age on the relationships of brown adipose tissue with sex and adiposity in humans. Diabetes. 2010; 59: 1789-93.

98. Kim Y, Kang BE, Ryu D, Oh SW, Oh CM. Comparative Transcriptome Profiling of Young and Old Brown Adipose Tissue Thermogenesis. Int J Mol Sci. 2021; 22.

99. Oberkofler H, Dallinger G, Liu YM, Hell E, Krempler F, Patsch W. Uncoupling protein gene: quantification of expression levels in adipose tissues of obese and non-obese humans. J Lipid Res. 1997; 38: 2125-33.

국 문 초 록

서론: 포도당 유사체인 [^{18}F]Fluoro-2-deoxyglucose ([^{18}F]FDG)를 이용한 양전자단층촬영 (Positron emission tomography, PET)은 지방 조직 내 포도당 섭취를 측정하여 가장 널리 제안되고 있는 진단 영상 기법이다. 그러나, [^{18}F]FDG-PET 은 뇌 또는 심장의 포도당 흡수가 높을수록 갈색 지방 조직 (interscapular brown adipose tissue, iBAT) 영상을 얻기에 어려움이 있다. 탈공역단백질 (Uncoupling protein 1, UCP1)은 미토콘드리아 내막에 위치하여 iBAT 의 바이오마커로 사용되며 최근에는 UCP1 발현을 실시간으로 모니터링 할 수 있는 리포터 마우스 (UCP1 reporter mouse, ThermoMouse)가 개발되었다. 전이체 단백질 (Translocator protein-18 kDa, TSPO)는 UCP1 과 함께 미토콘드리아 막에 위치하며 iBAT 에서 과 발현되어 있다. 이러한 근거로 갈색 지방 조직 특이적 영상을 위해 다양한 TSPO 표적 프로브들이 개발되었고 우리는 [^{18}F]fm-PBR28-d_2 를 사용하였다. 방사성 추적자 로부터 방출되는 체렌코프 방사선 (Cerenkov radiation, CR)을 사용하는 비침습적 체렌코프 발광 영상 (Cerenkov luminescence imaging, CLI)는 경제적이고 사용자 친화적인 장점으로 PET 의 대체 광학 이미징으로 이용되고 있다. 그러나, 갈색 지방 조직 영상에 있어서 [^{18}F]FDG 와 TSPO 표적 프로브를 이용한 PET 영상과 CLI 의 비교에 대한 연구는 아직까지 진행된 적이 없다. 따라서 우리는

갈색 지방 조직의 바이오마커인 UCP1 의 발현을 모니터링 할 수 있는 UCP1 리포터 마우스에서 [^{18}F]FDG 와 TSPO 표적 프로브를 이용하여 PET 영상과 CLI 를 비교 및 분석하고 PET 대체 옵션으로서 CLI 의 가능성을 평가하는 것을 목표로 한다.

방법: UCP1 리포터 마우스는 Luciferase2(Luc2)-T2A-tdTomato 카세트를 exon 1 의 Ucp1 코딩 서열 개시 코돈에 삽입하여 확립하였다. 발광 영상과 형광 영상은 IVIS 100 을 이용하여 수행하였다. 웨스턴 블릇과 조직화학염색 기법은 UCP1, Luciferase 와 TSPO 의 발현을 측정하기 위해 수행하였다. 갈색 지방 조직 내 UCP1 발현을 시각화 하기 위해 [^{18}F]FDG-PET/CLI 와 TSPO-PET/CLI 를 통해 평가하였다. [^{18}F]FDG 또는 [^{18}F]fm-PBR28-d_2 를 꼬리정맥주사 후 PET 스캔은 소동물 PET 영상 (small animal PET, SimPET)을 CLI 는 IVIS 100 을 이용하여 얻었다. PET 과 더불어 CLI 획득에 있어 비방사능 (molar activity, A_m)이 다른 TSPO 표적 프로브 간 iBAT 영상의 정성 및 정량적 차이를 조사하였다. 생리적 활성에 따른 iBAT 영상의 차이를 평가하기 위하여 추위 자극과 열중립 조건에서 4 시간 동안 사육한 뒤 PET 과 CLI 영상을 비교하였다. 마취 지속 시간에 따른 iBAT 영상의 차이를 확인하기 위하여 총 마취 시간을 2 시간 미만과 2 시간 이상의 그룹으로 나누어 PET 과 CLI 를 평가하였다. 모든 PET 영상은 AMIDE 이미징 소프트웨어를 이용해 재구성하고 정량분석 하였다. BLI, FLI 그리고 CLI 는 Living Imaging Software 를 이용하여 정량분석 하였다.

결과: 발광 및 형광 영상을 통하여 갈색 지방 조직 내 UCP1 발현을 관찰하였다. 갈색 지방 조직에서 UCP1, Luciferase 와 TSPO 가 다른 지방 조직에 비해 특이적으로 높은 발현과 단백질들 간의 상관성을 관찰할 수 있었다. [^{18}F]FDG-PET/CLI 의 신호들을 갈색 지방 조직에서 검출할 수 있었지만 뇌와 심장에서 더 높은 신호를 관찰하였다. 그러나 TSPO-PET/CLI 의 신호는 뇌와 심장에 섭취 없이 갈색 지방 조직에 강한 신호를 검출되었다. [^{18}F]FDG-PET/CLI 의 신호들은 내재성 UCP1 발현이 서로 다른 그룹에서의 차이를 관찰하기 어려웠다. 그러나 TSPO-PET/CLI 의 신호들은 내재성 UCP1 발현이 높은 그룹에서는 특이적으로 높았고 내재성 UCP1 발현이 낮은 그룹에서는 낮았다. 높은 비방사능을 가진 [^{18}F]fm-PBR28-d_2 을 이용한 PET 영상 및 CLI 모두 갈색 지방 조직에서 특이적인 신호를 검출되었다. 그러나 낮은 비방사능을 가진 [^{18}F]fm-PBR28-d_2 을 이용한 PET 영상 및 CLI 는 낮은 품질의 신호가 검출되었다. [^{18}F]FDG-PET/CLI 신호들은 추위 자극 그룹이 열 중립 조건 그룹보다 더 높은 신호를 보여주었다. 그러나 TSPO-PET/CLI 신호들은 [^{18}F]FDG 를 사용하는 것보다 추위 자극 그룹과 열 중립 조건 그룹 간의 더 민감하고 특이적인 차이를 관찰하였다. [^{18}F]FDG-PET/CLI 신호들은 마취 노출이 짧은 그룹과 긴 노출 그룹 간의 차이를 확인할 수 없었다. 흥미롭게도, TSPO-PET/CLI 신호들은 마취 노출이 짧은 그룹이 긴 노출 그룹보다 특이적으로 높았다.

결론: UCP1 리포터 마우스는 생체 내 갈색 지방 조직의 UCP1 발현을 모니터링 할 수 있는 유용한 모델이다. 이 연구는 최초로 갈색 지방 조직 표적 영상을 위해 [^{18}F]FDG 와 비교하여 TSPO 표적 프로브를 이용한 체렌코프 발광 영상을 평가하였다. 이러한 결과들은 TSPO 표적 프로브인 [^{18}F]fm-PBR28-d_2 는 [^{18}F]FDG 보다 갈색 지방 조직 영상을 위해 더 신뢰성 있고 민감한 프로브로 사용될 수 있음을 보여주었다. 나아가, TSPO 표적 프로브를 이용한 CLI 는 TSPO-PET 의 대체 광학 영상 옵션으로 사용될 수 있음을 시사한다.

주요어: 포도당 유사체, 양전자단층촬영법, 탈공역단백질 1, 전이체 단백질, 체렌코프 발광 영상, 탈공역단백질 1 리포터 마우스

Student number: 2017-25451